

Synthesis of atomically thin sheets by the intercalation-based exfoliation of layered materials

Received: 4 April 2022

Accepted: 15 December 2022

Published online: 13 February 2023

 Check for updates

Ruijie Yang^{1,2}, Yingying Fan^{1,2}, Liang Mei¹, Hyeon Suk Shin³,
Damien Voiry⁴, Qingye Lu², Ju Li⁵ & Zhiyuan Zeng^{1,6}

The intercalation-based exfoliation of layered materials is a broadly applicable strategy for the scalable production of atomically thin (from mono- to few-layer) sheets, including graphene, black phosphorus, hexagonal boron nitride and transition metal dichalcogenides. This strategy typically involves the intercalation of foreign species (ions or small molecules) into the interlayer spaces of layered materials, followed by a mild exfoliation process (spontaneously or via bath sonication, stirring or manual shaking). In this Review we introduce several intercalation-based exfoliation methods and highlight the factors that influence the quality of exfoliated nanosheets. In addition, we introduce the phase-transition phenomena involved in intercalation-based exfoliation, which may induce the resultant nanosheets to differ electronically and structurally from their bulk counterparts. Finally, we discuss potential commercial applications, focusing on devices (such as various electronic, photonic, photoelectric and energy devices) and catalysis (including photocatalysis and electrocatalysis).

Since the discovery of graphene¹ in 2004 there has been much research focused on the discovery of atomically thin (mono- to few-layer) sheets of other bulk materials (for example, black phosphorus (BP), hexagonal boron nitride (h-BN) and transition metal dichalcogenides (TMDs))². These atomically thin sheets have attracted interest in many fields including photonics, electronics, optoelectronics, energy storage, catalysis, environmental remediation and bioengineering³. The reliable production of atomically thin sheets is a frequent pursuit in academia and industry. Exfoliation, which is the direct isolation of atomic layers from the bulk layered crystal, is a powerful part of the synthetic toolkit⁴.

Exfoliation techniques, including micromechanical cleavage¹, direct liquid exfoliation⁵ and intercalation-based exfoliation⁶, are ‘top-down’ methods for the fabrication of atomically thin flakes from

their bulk counterparts. Micromechanical cleavage, which employs Scotch Tape to cleave layers from the bulk crystal, has a low production throughput, and the control over the thickness, size and shape of the targeted nanosheets is poor⁷. Direct liquid exfoliation in solvents, typically using sonication or shearing as a driving force, is also hampered by the low yield of the monolayer, as well as the small lateral size of the exfoliated flakes and the toxicity of the organic solvents used⁷. Intercalation-based exfoliation is amongst the most promising strategies for the mass production of atomically thin sheets, owing to its low energetic cost, solution-processability, scalability and the high yield of exfoliated monolayers with a large lateral size⁸. In the past decade, numerous intercalation-based exfoliation techniques have been developed, enabling the synthesis of many atomically thin materials (Fig. 1).

¹Department of Materials Science and Engineering and State Key Laboratory of Marine Pollution, City University of Hong Kong, Hong Kong, People's Republic of China. ²Department of Chemical and Petroleum Engineering, University of Calgary, Calgary, Alberta, Canada. ³Department of Chemistry, Ulsan National Institute of Science and Technology (UNIST), Ulsan, South Korea. ⁴Institut Européen des Membranes (IEM), UMR 5635, Université Montpellier, ENSCM, CNRS, Montpellier, France. ⁵Department of Nuclear Science and Engineering and Department of Materials Science and Engineering, Massachusetts Institute of Technology, Cambridge, MA, USA. ⁶Shenzhen Research Institute, City University of Hong Kong, Shenzhen, People's Republic of China. ✉ e-mail: liju@mit.edu; zhiyuzeng@cityu.edu.hk

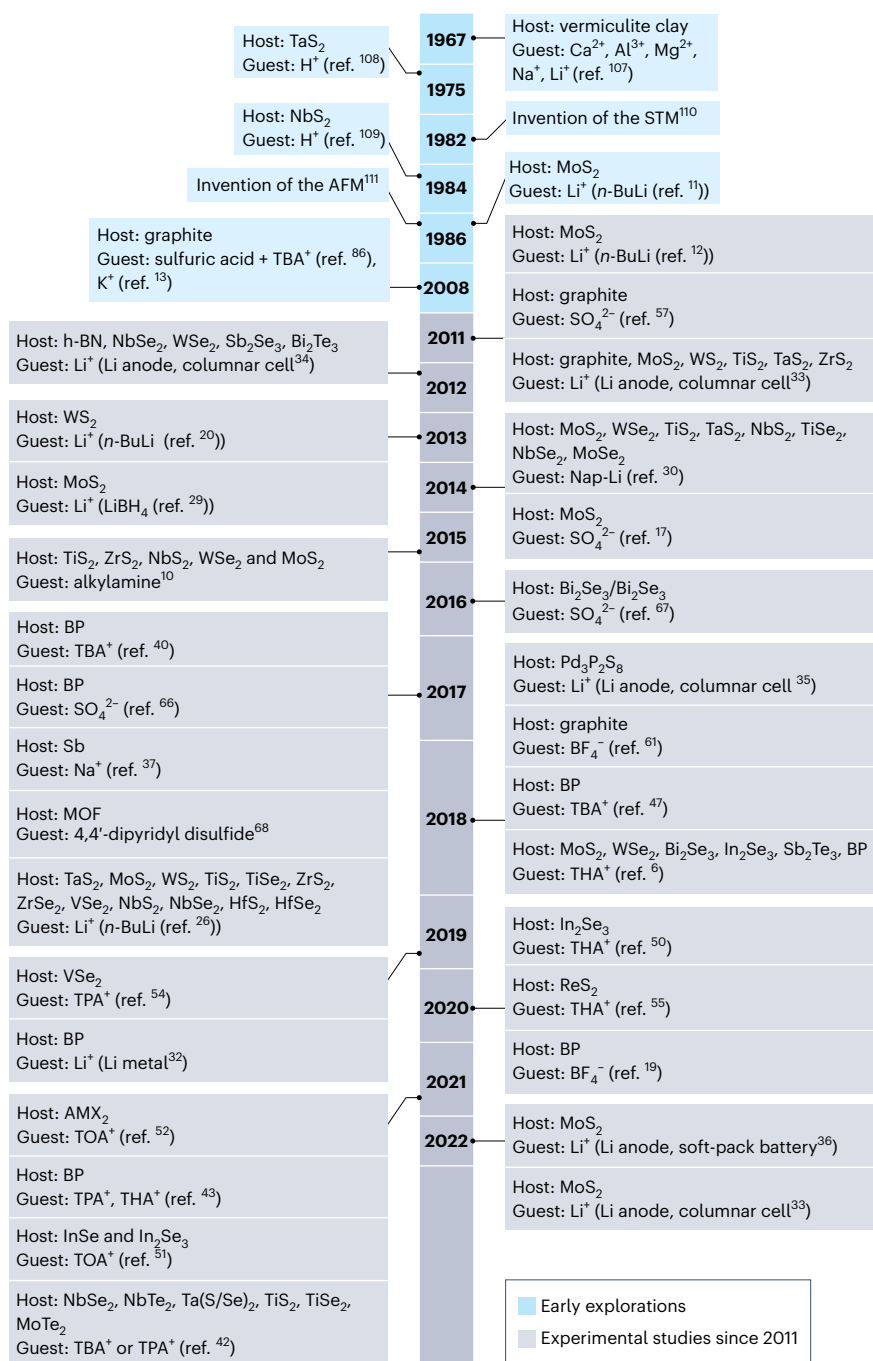


Fig. 1 | Timeline of key developments in the study of intercalation-based exfoliation for the synthesis of atomically thin sheets. Early attempts at intercalation-based exfoliation began in the 1960s; exfoliated objects included vermiculite clay, TaS₂ and NbS₂ (refs. 107–109). As a result of the limitation in the accuracy of the available characterization equipment (for example, the transmission electron microscope), it is difficult to determine whether or not monolayers were obtained in these studies. In the early 1980s, progress in electron microscope technology, such as the invention of the scanning tunnelling microscope (STM)¹¹⁰ and the atomic force microscope (AFM)¹¹¹, enabled the real-space imaging and accurate thickness measurement of exfoliated monolayers, paving the way for studies on intercalation-based exfoliation. In 1986, using *n*-butyllithium (*n*-BuLi) as the intercalant, the production of the MoS₂ monolayer was realized¹¹. In 2008, the isolation of graphene via intercalation-based exfoliation was achieved^{13,86}. Subsequently, research into intercalation-based exfoliation strategies grew in popularity along with the

production of a host of atomically thin sheets, which included graphene^{16,18,33,57–61}, TMDs^{6,10,12,17,20,24,26,27,29–31,33,34,36,42,54–56}, BP^{6,19,40,43,45,47,49,66}, h-BN³⁴, metal–organic frameworks (MOFs)⁶⁸, antimony (Sb)³⁸ and ternary palladium thiophosphate (Pd₃P₂S₈)³⁵, as well as materials with the formula A₂B₃ (where A is a group III element and B is a group VI element, such as In₂Se₃ (refs. 6,50,51), Bi₂Te₃ (ref. 34), Bi₂Se₃ (ref. 6), Sb₂Se₃ (ref. 34) and Sb₂Te₃ (ref. 6)) and the formula AMX₂ (where A is a monovalent metal, M is a trivalent metal and X is a chalcogen, such as AgCrS₂, AgCrSe₂, CuCrS₂, CuCrSe₂, NaCrS₂ (ref. 52)) and beyond^{94,95}. The past decade has also witnessed the richness of guest types, from cations (for example, the lithium ion (Li⁺)^{12,20,26,29,33–35} and tetraalkylammonium cations (R₄N⁺)^{40,43,45,51,52,54–56}) to anions (for example, the sulfate ion^{17,66} and the boron tetrafluoride ion^{19,61}) and molecules^{10,68}. TBA⁺, tetrabutylammonium; THA⁺, tetraheptylammonium; TOA⁺, tetracetylammmonium; TPA⁺, tetrapropylammmonium.

Still, this technique often introduces undesired basal-plane defects to the final product⁹, and may induce semiconducting-to-metallic phase transitions⁸.

The typical procedure of intercalation-based exfoliation involves the intercalation of a guest (a foreign species) and the subsequent exfoliation of the host (a layered material) (Fig. 2a). Guest intercalation can be achieved via chemical or electrochemical routes (Fig. 2b) and evidence for this is typically shown via a series of advanced characterization methods (Box 1). Host exfoliation refers to isolating atomic layers from the intercalation compound (host + guest) either spontaneously or using bath sonication, stirring or manual shaking (Fig. 2c), after which an opaque suspension of the exfoliated nanosheets is formed. In most cases, this process is accompanied by the formation of gas bubbles. At this stage the suspension typically contains incompletely peeled fragments, multilayered micro- and nanoparticles and guest molecules or ions beyond the isolated nanosheets. Thus, to obtain clean products, a purification process (Fig. 2d) is required, which encompasses a low-speed centrifugal process to remove the larger particles (which settle at the bottom of the vial), followed by high-speed centrifugation treatment with multiple cycles to release the guest molecules or ions from the surface of the isolated nanosheets. Subsequently, the collected sediment, which is rich in two-dimensional (2D) nanosheets (purified nanosheets), is often redispersed in water or other solvent (for example, isopropyl alcohol, *N,N*-dimethylformamide) via sonication to form a printable ink for storage and later use.

In this Review, we introduce several intercalation-based exfoliation strategies, with a focus on the relevant chemistries and final products (Table 1; Supplementary Figs. 1 and 2), as well as the merits and demerits of each strategy, aiming to provide a guide for the synthesis of atomically thin sheets.

Mechanism of intercalation-based exfoliation

For intercalation-based exfoliation to be successful, the interlayer adhesion of layered materials must be overcome via intercalation and post-intercalation effects, which facilitate the subsequent delamination of atomic layers. Such post-intercalation effects can be the increase in the interlayer distance¹⁰, the release of bubbles^{11,12} or energetically favourable solvation^{13,14}. This depends critically on the type of intercalant and solvent used.

Intercalation by molecules (for example, alkylamine¹⁰) is a charge-transfer-free process and normally results in a substantial increase in the layer spacing. Such a post-intercalation effect weakens the van der Waals forces that cause interlayer adhesion, facilitating delamination of the atomic layers. Alternatively, intercalation by ions (for example, alkali metal ions^{11–14}), whether via chemical or electrochemical routes, always occurs with charge transfer between the intercalated ions and layered crystals, inducing the formation of charged layers. Such a process decreases the interlayer van der Waals forces but produces additional electrostatic attraction forces (which are stronger than the van der Waals forces¹⁵) between oppositely charged ions and layers. As a result, the overall attraction between the layers increases. The overcoming of such overall attractions are often related to the solvent used during the exfoliation process. Protic solvents (such as water) usually cause gas release (for example, hydrogen^{11,12}, sulfur dioxide^{16,17} and oxygen^{18,19}), which creates a large force, pushing individual layers apart, playing a strong role in the exfoliation mechanism. Aprotic solvents can coordinate the charged layers and ions, thereby facilitating dispersion (energetically favourable solvation) and therefore isolation of the atomic layers^{13,14}.

Lithium-ion intercalation-based exfoliation strategies

Since the seminal report in 1986¹¹, Li⁺ (ionic radius 0.76 Å) intercalants have been applied extensively in the intercalation-based exfoliation of atomically thin sheets. Several Li⁺ intercalants are available and are introduced here.

n-Butyllithium

n-Butyllithium (*n*-BuLi) is a commonly used Li⁺ intercalant^{12,20–27}. Typically, this intercalation (equation (1), Table 1) is realized via immersing the bulk layered material in a stoichiometric *n*-BuLi hexane solution using an argon-filled glovebox and stirring at 100 °C for around 2–3 days. After full intercalation and transfer of the intercalation compound into water, exfoliation is achieved under the action of hydration (often creating hydrogen gas; equation (2)) and sonication¹² or shaking²⁶.

Intercalation-based exfoliation using *n*-BuLi is a commonly used method, but the long intercalation time (~2–3 days) and harsh intercalation conditions (100 °C, argon-filled glovebox) are limitations. This method is used mainly to exfoliate TMD materials (MoS₂ in particular^{12,21–25,27}) (Fig. 3a), producing monolayers in high yield, although it is often accompanied by a phase transition from hexagonal (2H) to octahedral/distorted octahedral (1T/1T'), respectively). In addition, the highly flammable nature of *n*-BuLi brings safety concerns.

Lithium borohydride

Lithium borohydride (LiBH₄) can also act as a Li⁺ intercalant^{28,29}. Notably, this intercalation (equation (3), Table 1) is a solvent-free process, which is achieved by keeping the mixed powders (LiBH₄ and the bulk layered material) at 300 °C for ~2–3 days in an argon-filled glovebox. After hydration (equation (4)) and sonication-assisted exfoliation processes, atomically thin sheets can be produced.

Intercalation-based exfoliation using LiBH₄ is relatively safe, owing to the use of a solid-state approach, although a long intercalation time (~2–3 days) and harsh intercalation conditions (300 °C, argon-filled glovebox) are needed. This method was first demonstrated for the exfoliation of WS₂ (ref. 28), then for MoS₂ (ref. 29), yielding 1T-WS₂ and 1T-MoS₂ monolayers, respectively. Although this method is effective for isolating TMD monolayers, it still involves a phase transition.

Naphthalenide lithium

Naphthalenide lithium (Nap-Li), a more reductive organolithium reagent than *n*-BuLi, can be used as a Li⁺ intercalant³⁰. Its strong reduction capacity leads to irreversible chemical decomposition of the layered crystal if it is reacted directly with it. To avoid crystal decomposition, before Li⁺ intercalation, a hydrazine (N₂H₄) pre-intercalation step is needed under hydrothermal conditions (130 °C, 2 days), during which the layered crystals are pre-expanded via intercalation (equation (5), Table 1), partial oxidation (equation (6)) and the decomposition and gasification (equation (7)) of N₂H₄. After the pre-intercalation step, immersing the pre-expanded crystals in an anhydrous tetrahydrofuran solution of Nap-Li (that is, Li-C₁₀H₈ in Table 1) and stirring for 5 h in an argon-filled glovebox achieves Li⁺ intercalation (equation (8)) before hydration (equation (9)), after which mild sonication-driven exfoliation gives the atomically thin materials.

Intercalation-based exfoliation using Nap-Li provides a universal strategy for the production of a wide range of TMD nanosheets, including MoS₂, WS₂, TiS₂, TaS₂, NbS₂, TiSe₂, NbSe₂ and MoSe₂ (ref. 30). Most of the exfoliated MoS₂ flakes are monolayers (up to 90%), although phase transition (from 2H to 1T) still occurs³⁰. This strategy is time-consuming (~3 days) and inconvenient owing to the need for two synthetic steps. In addition, crystal decomposition and the emission of hazardous gases (ammonia, hydrogen) are common side effects.

Pyrene lithium

Recently, a rapid and mild Li⁺ intercalation route has been demonstrated via the use of pyrene lithium (Py-Li) as a Li⁺ intercalant³¹. Impressively, this intercalation (equation (10), Table 1) can be achieved within 1 h at room temperature. Such a rapid intercalation rate is attributed to the large potential gap between Py-Li and the layered crystal MoS₂ ($\Delta U^{\text{eq}} = 0.27$ V), providing a large driving force for spontaneous electron

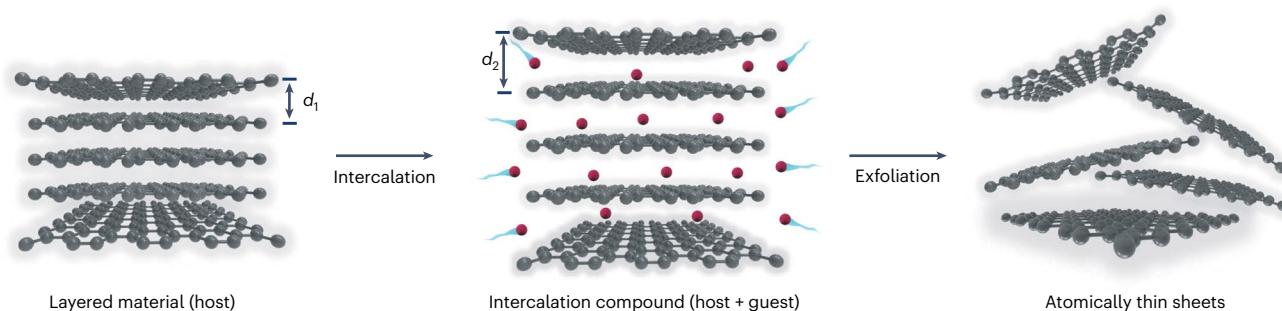
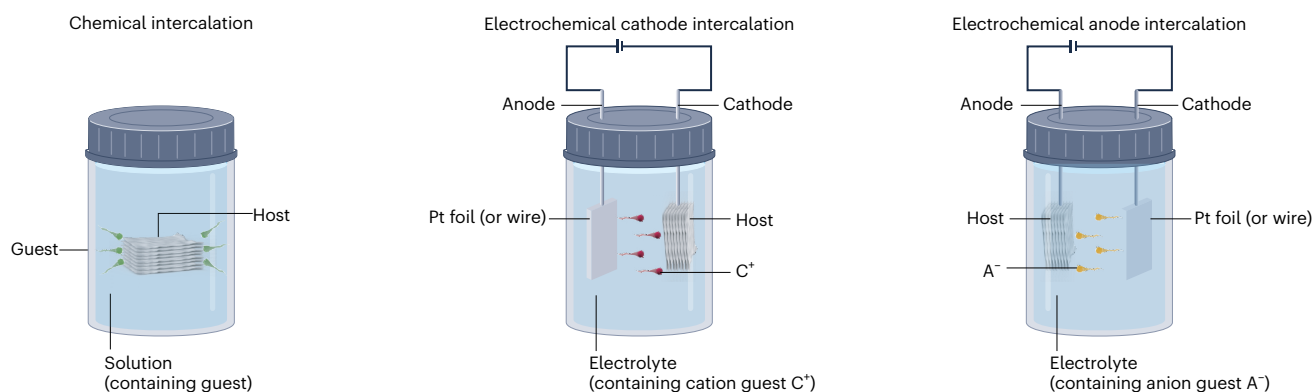
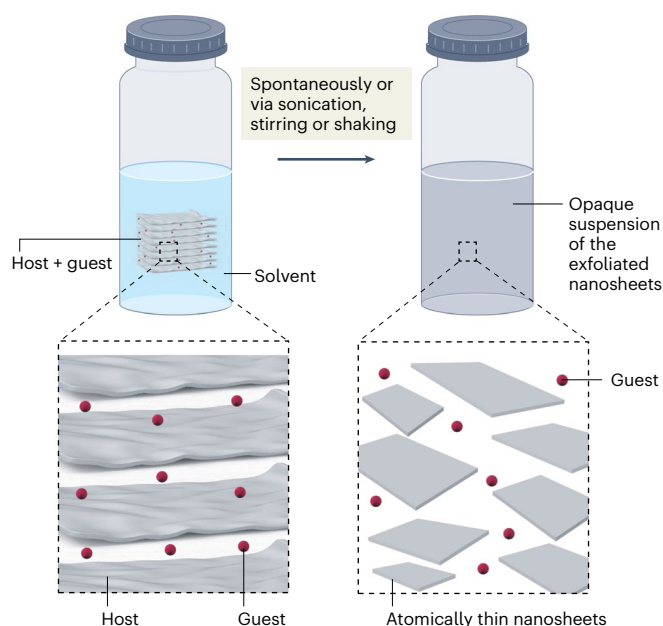
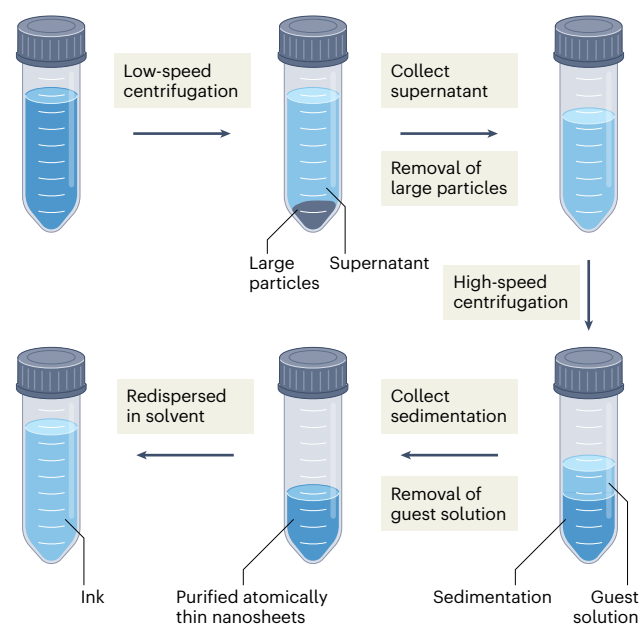
a Intercalation-based exfoliation**b Intercalation****c Exfoliation****d Purification**

Fig. 2 | Schematic illustration of intercalation-based exfoliation. **a**, Typical procedure of intercalation-based exfoliation. The red spheres represent the intercalant species (also called the guest); d_1 represents the original interlayer distance and d_2 represents the interlayer distance after intercalation, where $d_2 > d_1$. **b**, Intercalation routes (chemical intercalation, electrochemical cathode intercalation and electrochemical anode intercalation). Typically, chemical intercalation (left) is realized by immersing the bulk layered material (the host) into an intercalant solution for a specific time period under specific conditions. Electrochemical cathode intercalation (middle) is performed using an electrochemical cell with platinum (Pt) foil (or wire) as the anode, the bulk layered material as the cathode and a solution containing the intercalating cation

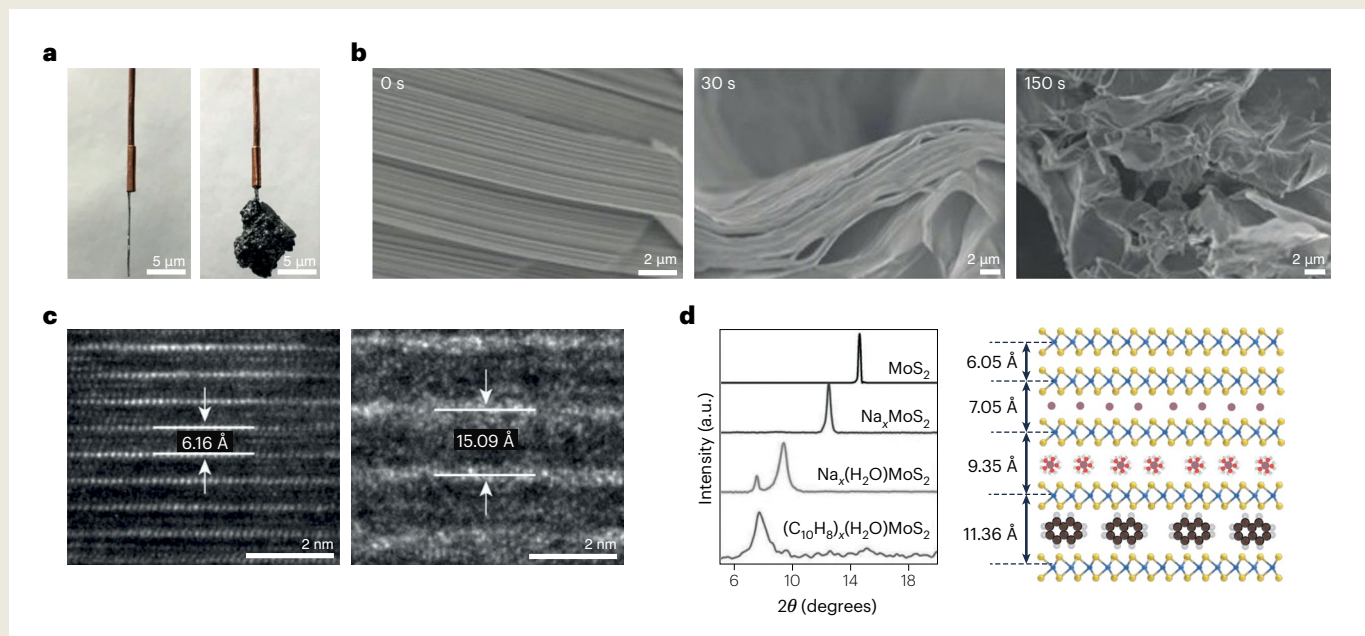
guest as the electrolyte. Electrochemical anode intercalation (right) is performed using an electrochemical cell with Pt foil (or wire) as the cathode, the bulk layered material as the anode and a solution containing the intercalant anion guest as the electrolyte. Electrochemical intercalation is realized by applying an appropriate voltage to the electrochemical cell for a period of time. **c**, Exfoliation process. After full intercalation, the intercalation compound (host + guest) is transferred into water or other solvent, and sonication, stirring or shaking is performed, isolating the atomic layers and forming an opaque suspension of the exfoliated nanosheets. **d**, Purification treatment, performed via low-speed centrifugation in series with high-speed centrifugation (with several cycles) to purify and collect the exfoliated nanosheets.

BOX 1

An introduction of the characterization of intercalation

Intercalation, a key process before exfoliation, is normally recorded directly via digital photographs⁶ (see **a**). In these images, volume expansion is a typical sign of intercalation. Scanning electron microscopy (SEM) is another common tool to record intercalation at different periods⁴⁰ (**b**). An increase in the interlayer spacing caused by intercalation can be seen in such SEM images. Transmission electron microscopy (TEM), a sophisticated subnanometre-resolution imaging technology, provides the means to accurately detect the increased interlayer distance¹⁰⁴ (**c**). X-ray diffraction (XRD) can also be used to calculate interlayer distances³⁰ (**d**). Atomic force microscopy and Raman spectroscopy can also provide interlayer-distance information¹⁰⁴, although they are not as commonly used as TEM and XRD.

The elemental composition of intercalated species can be examined via energy-dispersive X-ray spectroscopy¹⁰⁴. The amount of intercalation is typically analysed using nuclear magnetic resonance (NMR)⁴². Intercalation often causes phase transitions, and X-ray photoelectron spectroscopy (XPS) and Raman spectroscopy offer means to probe this phenomenon¹⁰⁴. Intercalation also leads to changes in the electronic and optical properties. Photoluminescence is a tool to analyse these properties¹⁰⁴. Density functional theory (DFT) calculations are often used to verify or predict changes in these properties via the simulated electronic structures of pristine materials and intercalation compounds¹⁰⁴.



Characterization of intercalation. **a**, Digital photographs of a MoS₂ crystal before (left) and after (right) the intercalation of tetraheptylammonium bromide. **b**, SEM images of a BP crystal before (left) and after (middle and right) various periods of tetra-*n*-butylammonium bisulfate intercalation.

c, Cross-sectional TEM images of a BP crystal before (left) and after (right) cetyltrimethylammonium bromide intercalation. **d**, XRD patterns (left) and schematics of MoS₂ (right) before and after intercalation.

Panels adapted with permission from: **a**, ref. ⁶, Springer Nature Ltd; **b**, ref. ⁴⁰, Wiley; **c**, ref. ¹⁰⁴, Springer Nature Ltd; **d**, ref. ³⁰ under a Creative Commons licence CC BY.

migration. Undergoing hydration (equation (11)) and sonication-driven exfoliation, MoS₂ monolayers with a yield of 80% are obtained. In spite of the phase transition of the final products, this method has the potential for the mass production of TMD monolayers due to the speed of intercalation.

Lithium metal

Lithium metal can be used as the source for Li⁺ intercalation-based exfoliation processes³² and has been demonstrated for the production of BP monolayers³². Typically, this fabrication process undergoes several steps in series, and includes outgassing of the BP layered crystal (at 100 °C under dynamic vacuum), mixing of the BP layered crystal and lithium metal (with a stoichiometric ratio of Li/P = 1/8), cooling (-50 °C), the addition of ammonia gas (to dissolve lithium), standing (lithium intercalation, 24 h), the removal of ammonia, drying of the

intercalation compound, the addition of an anhydrous aprotic solvent and, finally, sonication (1 h) or stirring (one week) for exfoliation.

This method results in stable, uniform, predominantly monolayer, flexible BP nanoribbons with typical widths of 4–50 nm and lengths of up to 75 μm (Fig. 3b). However, the disadvantage of this method lies in its complex, time-consuming and demanding operation requirements. It is of note that, due to the moisture/air sensitivity of lithium metal, the sealing of the setup – to maintain a vacuum or inert atmosphere – must be strictly maintained throughout the process.

Lithium-ion anode

Alternatively, Li⁺ intercalation can be achieved via electrochemical paths^{8,33,34}, performed using an electrochemical cell containing a Li-metal foil anode, a lithium hexafluorophosphate (LiPF₆) in ethyl carbonate (EC) and dimethyl carbonate (DMC) solution electrolyte

Table 1 | A list of several credible intercalation-based exfoliation strategies

| Strategy | Intercalation and exfoliation chemistry | Equation | Products | |
|----------------------------------|---|--|---|---|
| Li ⁺ IE | <i>n</i> -BuLi | $\text{MoS}_2 + x\text{Li} \cdot [n\text{-C}_4\text{H}_9] \rightarrow \text{Li}_x\text{MoS}_2 + \frac{x}{2} n\text{-C}_8\text{H}_{18}$ | (1) | TMDs ²⁶ (in particular MoS ₂ (refs. ^{12,21–25,27}), Bi ₁₂ O ₁₇ Cl ₂ (ref. ⁹²), ZnIn ₂ S ₄ (ref. ⁹⁴) and Ni ₃ Cr ₂ P ₂ S ₈ (ref. ⁹⁸)) |
| | | $\text{Li}_x\text{MoS}_2 + x\text{H}_2\text{O} \rightarrow \frac{x}{2}\text{H}_2 + x\text{LiOH} + \text{MoS}_2$ | (2) | |
| | LiBH ₄ | $\text{MoS}_2 + x\text{LiBH}_4 \rightarrow \text{Li}_x\text{MoS}_2 + \frac{x}{2}\text{B}_2\text{H}_6 + \frac{x}{2}\text{H}_2$ | (3) | WS ₂ (ref. ²⁸) and MoS ₂ (ref. ²⁹) |
| | | $\text{Li}_x\text{MoS}_2 + x\text{H}_2\text{O} \rightarrow \frac{x}{2}\text{H}_2 + x\text{LiOH} + \text{MoS}_2$ | (4) | |
| | Nap-Li | $\text{MoS}_2 + x\text{N}_2\text{H}_4 \rightarrow (\text{N}_2\text{H}_4)_x\text{MoS}_2$ | (5) | TMDs (including MoS ₂ , WS ₂ , TiS ₂ , TaS ₂ , NbS ₂ , TiSe ₂ , NbSe ₂ and MoSe ₂) ³⁰ |
| | | $(\text{N}_2\text{H}_4)_x\text{MoS}_2 + x\text{H}_2\text{O} \rightarrow x\text{N}_2\text{H}_5^+ + x\text{OH}^- + \text{MoS}_2$ | (6) | |
| | | $2\text{N}_2\text{H}_5^+ + 2\text{OH}^- \rightarrow \text{H}_2 + \text{N}_2 + 2\text{NH}_3 + 2\text{H}_2\text{O}$ | (7) | |
| | | $\text{MoS}_2 + x\text{Li-C}_{10}\text{H}_8 \rightarrow \text{Li}_x\text{MoS}_2 + x\text{C}_{10}\text{H}_8$ | (8) | |
| | | $\text{Li}_x\text{MoS}_2 + x\text{H}_2\text{O} \rightarrow \frac{x}{2}\text{H}_2 + x\text{LiOH} + \text{MoS}_2$ | (9) | |
| Py-Li | $\text{MoS}_2 + x\text{Li-Py} \rightarrow \text{Li}_x\text{MoS}_2 + x\text{Py}$ | (10) | MoS ₂ (ref. ³¹) | |
| | $\text{Li}_x\text{MoS}_2 + x\text{H}_2\text{O} \rightarrow \frac{x}{2}\text{H}_2 + x\text{LiOH} + \text{MoS}_2$ | (11) | | |
| Li anode | $\text{Li}^+ + \text{MoS}_2 + e^- \rightarrow \text{Li}_x\text{MoS}_2$ | (12) | Graphene, MoS ₂ , WS ₂ , TiS ₂ , TaS ₂ , ZrS ₂ , h-BN, NbSe ₂ , WSe ₂ , Sb ₂ Se ₃ , Bi ₂ Te ₃ (refs. ^{8,33–36}), Pd ₃ P ₂ S ₈ (ref. ³⁵) and BiOCl (ref. ³⁹) | |
| | $\text{Li}_x\text{MoS}_2 + x\text{H}_2\text{O} \rightarrow \frac{x}{2}\text{H}_2 + x\text{LiOH} + \text{MoS}_2$ | (13) | | |
| R ₄ N ⁺ IE | $\text{MoS}_2 + x\text{R}_4\text{N}^+ + xe^- \rightarrow (\text{R}_4\text{N}^+)_x\text{MoS}_2$ | (14) | Graphene ^{44,46,53} , TMDs ^{6,42,54–56,97} , BP ^{40,43,45,47,49} , A ₂ B ₃ (such as In ₂ Se ₃ (refs. ^{6,50,51}), Bi ₂ Se ₃ (ref. ⁶) and Sb ₂ Te ₃ (ref. ⁶)), AMX ₂ (ref. ⁵²) and PdSeO ₃ (ref. ⁴¹) | |
| | $(\text{R}_4\text{N}^+)_x\text{MoS}_2 \rightarrow (\text{R}^+)_x\text{MoS}_2 + \text{R}_3\text{N}$ | (15) | | |
| | $(\text{R}^+)_x\text{MoS}_2 + xe^- \rightarrow (\text{R}^-)_x\text{MoS}_2$ | (16) | | |
| | $(\text{R}^-)_x\text{MoS}_2 + x\text{H}_2\text{O} \rightarrow x\text{RH} + x\text{OH}^- + \text{MoS}_2$ | (17) | | |
| SO ₄ ²⁻ IE | $\text{H}_2\text{O} - e^- \rightarrow \text{H}^+ + \text{HO}^\cdot$ | (18) | Graphene ^{16,57–59} , MoS ₂ (ref. ¹⁷), BP ⁶⁶ and A ₂ B ₃ (Bi ₂ Se ₃ and Bi ₂ Te ₃) ⁶⁷ | |
| | $\text{HO}^\cdot - e^- \rightarrow \text{H}^+ + \text{O}^\cdot$ | (19) | | |
| | $\text{MoS}_2 + x\text{SO}_4^{2-} + y\text{HO}^\cdot + z\text{O}^\cdot \rightarrow (\text{SO}_4^{2-})_x(\text{HO}^\cdot)_y(\text{O}^\cdot)_z\text{MoS}_2$ | (20) | | |
| | $4(\text{SO}_4^{2-})_x(\text{HO}^\cdot)_y(\text{O}^\cdot)_z\text{MoS}_2 \rightarrow 4x\text{SO}_2 + (2x + 2z + y)\text{O}_2 + 2y\text{H}_2\text{O} + 8xe^- + 4\text{MoS}_2$ | (21) | | |
| BF ₄ ⁻ IE | $\text{H}_2\text{O} - e^- \rightarrow \text{H}^+ + \text{HO}^\cdot$ | (22) | Graphene ^{18,60,61} and BP ¹⁹ | |
| | $\text{HO}^\cdot - e^- \rightarrow \text{H}^+ + \text{O}^\cdot$ | (23) | | |
| | $\text{MoS}_2 + x\text{BF}_4^- + y\text{HO}^\cdot + z\text{O}^\cdot \rightarrow (\text{BF}_4^-)_x(\text{HO}^\cdot)_y(\text{O}^\cdot)_z\text{MoS}_2$ | (24) | | |
| | $4(\text{BF}_4^-)_x(\text{HO}^\cdot)_y(\text{O}^\cdot)_z\text{MoS}_2 \rightarrow 4x\text{HBF}_4 + (x + 2z + y)\text{O}_2 + (2y - 2x)\text{H}_2\text{O} + 4xe^- + 4\text{MoS}_2$ | (25) | | |
| Molecule IE | DPDS | $\text{C}_{10}\text{H}_8\text{N}_2\text{S}_2 \rightarrow 2\text{C}_5\text{H}_4\text{NS}$ | (26) | MOF ⁶⁸ |
| | Alkylamine | – | – | TiS ₂ , ZrS ₂ , NbS ₂ and MoS ₂ (ref. ¹⁰) |

IE, intercalation-based exfoliation; DPDS, 4,4'-dipyridyl disulfide.

and with the bulk layered materials for exfoliation coated onto a copper (Cu) foil cathode^{8,33,34}. After a galvanostatic discharge process (Li⁺ intercalation, equation (12) in Table 1) for 6 h at room temperature, followed by sonication-assisted exfoliation along with a hydration process (equation (13)), the target nanosheets are obtained.

The electrochemical Li⁺ intercalation-based exfoliation strategy is generic. Using this strategy, a library of mono- or few-layer inorganic nanosheets have been produced, including graphene, MoS₂, WS₂, TiS₂, TaS₂, ZrS₂, h-BN, NbSe₂, WSe₂, Sb₂Se₃, Bi₂Te₃, Pd₃P₂S₈ and beyond (Fig. 3c,d)^{8,33–36}. The yield of MoS₂ and TaS₂ monolayers can reach 92% and 93%, respectively⁸; the produced ultrasmall Pd₃P₂S₈ nanosheets (lateral size ≈ 2.3 nm, thickness ≈ 1.1 nm) undergo a phase transformation from crystalline to amorphous, which activates the electrochemically inert bulk crystal material, making it an efficient electrocatalyst for hydrogen evolution reactions (HERs)³⁵. Another strength of this method comes from the ability to monitor and finely control the degree of Li⁺ insertion via tuning of the cutoff voltage (Fig. 3e)⁸, which avoids incomplete or excessive lithium insertion. This strategy is also scalable. The output of a single electrochemical cell has been developed from

the initial milligram level (using a columnar cell^{33,34} or a coin cell⁸) to the gram scale (using a soft-pack battery³⁶) (Fig. 3f). In the future, if technology allows, it is expected that a tonne output will be achieved by expanding the scale of the electrochemical cell⁸.

A similar strategy can be used based on the electrochemical intercalation of sodium ions (Na⁺) or potassium ions (K⁺)^{37–39}. This intercalation process is carried out using an alkali metal salt solution (for example, Na₂SO₄ (refs. ^{37,38}) or KCl (ref. ³⁹)) with the bulk layered material as the cathode and a Pt wire or foil as the anode under a constant voltage. The resulting intercalated compounds are exfoliated via a short sonication period (0.5–1 min) in water as before, yielding mono- or few-layer sheets. Impressively, this method shows good applicability in the preparation of atomically thin antimonene (Sb) flakes^{37,38}.

Tetraalkylammonium-ion intercalation-based exfoliation strategies

The R₄N⁺ cation (for example, tetramethylammonium (TMA⁺)⁴⁰, tetraethylammonium (TEA⁺)^{40,41}, tetrapropylammonium (TPA⁺)^{42,43}, tetrabutylammonium (TBA⁺)^{40,42,44–49}, tetraheptylammonium (THA⁺)^{6,50,51} and

tetraoctylammonium (TOA⁺)⁵²; see Supplementary Table 1 for the structural formulae) is a popular intercalant for the electrochemical exfoliation of layered crystals. Intercalation is performed by applying a voltage (between -5 and -10 V) in an electrochemical cell with a bulk crystal cathode, a Pt wire or foil anode and an R₄N⁺-containing electrolyte. During this intercalation process, the insertion of R₄N⁺ (equation (14) in Table 1) contributes to a preliminary expansion of the crystal. Electrochemical decomposition of R₄N⁺ (equations (15) and (16)) with gas release (for example, an alkane, in equation (17)) amplifies the rapid and considerable volume expansion. Following intercalation, atomic layers can be isolated spontaneously⁴⁹ or assisted by sonication⁴².

The superiority of this strategy lies in its universality. A wide range of atomically thin materials can be produced via this strategy, including graphene^{44,46,53}, TMDs^{6,42,54–56}, BP^{40,43,45,47,49}, A₂B₃-type materials (such as In₂Se₃ (refs. ^{6,50,51}), Bi₂Se₃ (ref. ⁶) and Sb₂Te₃ (ref. ⁶)), AMX₂-type materials (such as AgCrS₂, AgCrSe₂, CuCrS₂, CuCrSe₂ and NaCrS₂)⁵² and beyond.

Electrochemical R₄N⁺ intercalation-based exfoliation tends to yield less defective graphene in comparison with anion intercalation-based exfoliation (using sulfate ions, for instance), owing to its non-oxidative production route^{44,46}. The exfoliated graphene, however, is unstable and is easily restacked into graphite⁴⁶. Thus, the covalent functionalization of graphene is often needed to improve its stability⁴⁶. In contrast to the TMD monolayers exfoliated using Li⁺ intercalation-based techniques (with defects, small in size and associated phase transitions)^{12,33}, TMD monolayers produced via R₄N⁺ intercalation-based exfoliation are generally defect-free, phase-transition-free, large in size and environmentally stable^{6,42,54–56} (Fig. 4a,b).

The properties of atomically thin BP exfoliated via this strategy are dependent on the R₄N⁺ size. The smaller-sized TPA⁺ intercalant typically yields BP nanoribbons⁴³, whereas larger-sized TBA⁺ and THA⁺ result in the production of BP nanosheets^{40,45,47,49}. This difference is related to the anisotropic in-plane bond energies of the BP crystal, resulting from the non-equivalent P=P covalent bonds along two vertical directions: the armchair (AC) direction ($L_{AC} = 2.224 \text{ \AA}$) and the zigzag (ZZ) direction ($L_{ZZ} = 2.244 \text{ \AA}$) (Fig. 4c). Intercalation of small-sized TPA⁺ leads to a small lattice strain, which tends to create a fissure along the ZZ direction. Such fissures open up BP like a zip, forming BP nanoribbons (Fig. 4d,e). However, excessive strain induced by the intercalation of large-sized TBA⁺ or THA⁺ may override the P=P bond energy differences in the ZZ and AC directions, leading to non-directional exfoliation. Such unordered exfoliation creates BP nanosheets. Impressively, such yielded BP nanosheets are non-oxidative⁴⁷, defect-free⁴⁰ and layer-tunable (via changing the applied potential)⁴⁵. This strategy provides an opportunity for the ultrafast production (in minutes)⁴⁷ of BP nanosheets with an ultralarge average domain size (~80 μm)⁴⁹.

Anion intercalation-based exfoliation strategies

Various polyanions have also been demonstrated as intercalation ions for the synthesis of atomically thin sheets, including SO₄²⁻ (refs. ^{16,57–59}), BF₄⁻ (refs. ^{18,60,61}), ClO₄⁻ (ref. ⁶²), PO₄³⁻ (ref. ⁶³), C₂O₄²⁻ (ref. ⁶³), OH⁻ (ref. ⁶⁴)

and RSO₃⁻ (ref. ⁶⁵). They are typically exploited for the production of graphene. Here, we limit our discussion to SO₄²⁻ and BF₄⁻, the most common examples.

Sulfate ion

The sulfate ion (SO₄²⁻), can electrochemically intercalate bulk crystals using an electrochemical cell containing a bulk layered crystal anode, Pt wire (or foil) cathode and an SO₄²⁻-containing electrolyte (such as H₂SO₄ (refs. ^{57,58,66}), Na₂SO₄ (refs. ^{16,17,67}), K₂SO₄ (ref. ¹⁶) and (NH₄)₂SO₄ (ref. ¹⁶)). The working principles of this electrochemical intercalation are as follows: (1) water oxidation at the anode under a voltage of +10 V promotes the formation of hydroxyl ions or radicals (equations (18) and (19) in Table 1), which attack the bulk layered materials, thereby inducing the depolarization and expansion of the layers, as well as the intercalation of SO₄²⁻ (equation (20)); and (2) the intercalated SO₄²⁻ as well as the HO[•] and O[•] radicals undergo a redox reaction to release gaseous species (for example, sulfur dioxide, oxygen), facilitating the further enhancing of the interlayer spaces (equation (21)). After a mild sonication treatment, target flakes are yielded.

The electrochemical SO₄²⁻ intercalation-based exfoliation strategy is an efficient and popular method for the exfoliation synthesis of graphene^{16,57–59}, but often introduces basal-plane defects, which result from surface oxidation. Beyond graphene, this strategy has the potential to produce other inorganic nanosheets, such as MoS₂ (ref. ¹⁷), BP⁶⁶ and topological insulators (Bi₂Se₃ and Bi₂Te₃)⁶⁷. However, the monolayer yield of the final products is relatively low; for example, the yield of the MoS₂ monolayer is below 7% (ref. ¹⁷).

Boron tetrafluoride ion

The boron tetrafluoride ion (BF₄⁻) is another commonly used anion for electrochemical exfoliation. Both the cell configuration and the intercalation principles (equations (22)–(25)) of this strategy are similar to electrochemical SO₄²⁻ intercalation-based exfoliation. This strategy is also mainly applied to the production of graphene^{18,60,61}. Impressively, the exfoliated graphene can realize fluorine functionalization⁶¹, improving the thermal stability and transparency of graphene. Beyond graphene, BP monolayers can also be produced using this method via an oxygen-driven exfoliation mechanism¹⁹. However, the final BP monolayers contain lots of neutral defects and dangling oxygen and hydrogen bonds at the edges (Fig. 4f)¹⁹.

Molecular intercalation-based exfoliation strategies

Atomically thin flakes can also be exfoliated by intercalating molecules (for example, 4,4'-dipyridyl disulfide and alkylamines) into the bulk materials to widen their interlayer distances^{10,68}.

4,4'-Dipyridyl disulfide

4,4'-Dipyridyl disulfide, a chemically labile dipyridyl ligand, has been demonstrated as a molecular intercalant for the exfoliation of MOFs

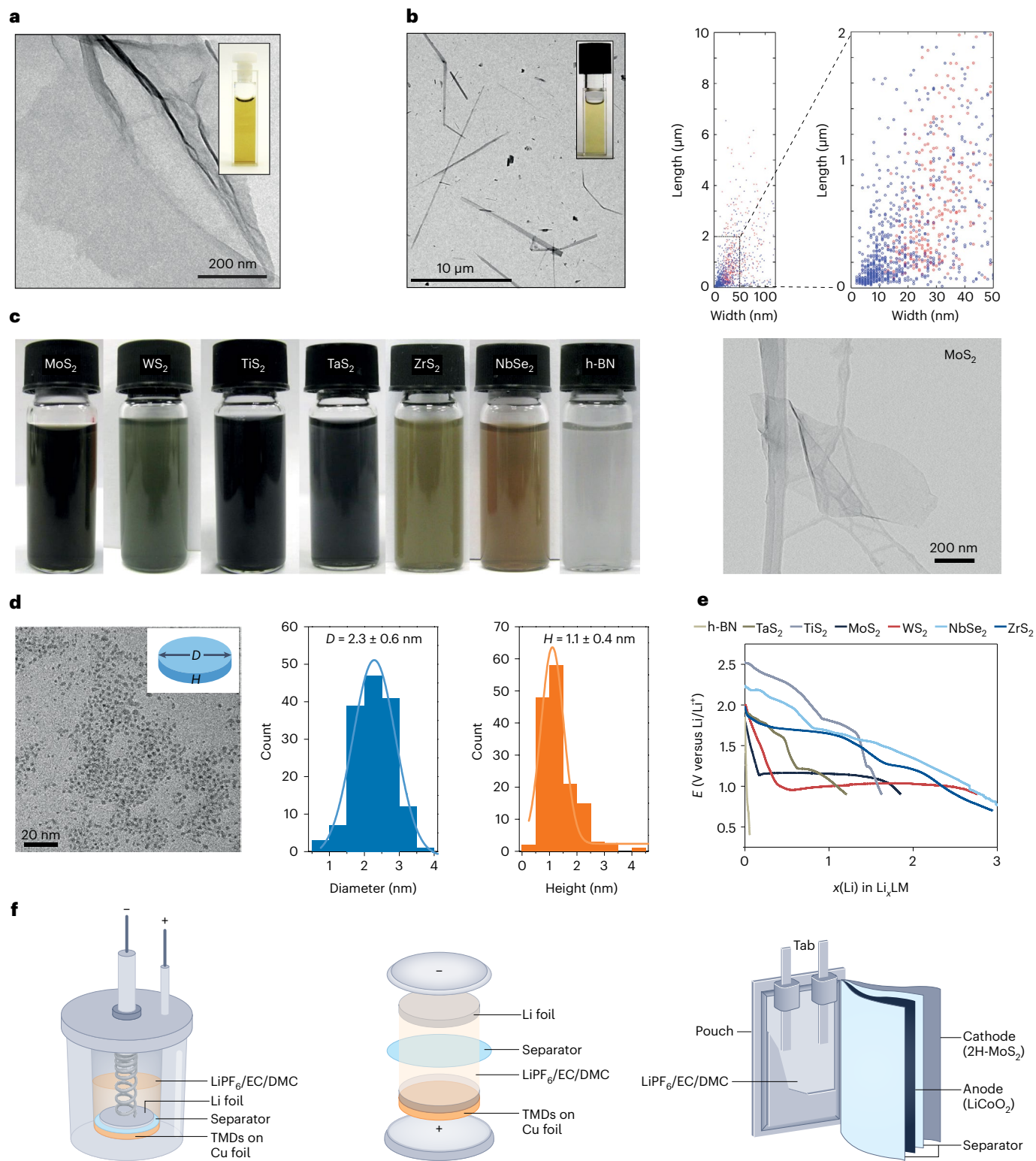
Fig. 3 | Li⁺ intercalation-based exfoliation. **a**, TEM image of a MoS₂ monolayer fabricated via intercalation-based exfoliation using *n*-BuLi as the intercalant. Inset: photograph of an exfoliated MoS₂ suspension in water. **b**, BP nanoribbons fabricated via intercalation-based exfoliation using lithium metal as the intercalant. Left: TEM image of the exfoliated BP nanoribbons, where the inset shows a photograph of an exfoliated BP suspension. Right: scatterplots of length versus width for the exfoliated BP nanoribbons, as extracted from the TEM data. The right-hand panel shows an enlarged view of the area indicated. Blue symbols denote sonication-driven exfoliation; red symbols denote spontaneous exfoliation. **c**, Inorganic nanosheets fabricated via electrochemical Li⁺ intercalation-based exfoliation. Left: photographs of suspensions of exfoliated MoS₂, WS₂, TiS₂, TaS₂, ZrS₂, NbSe₂ and h-BN. Right: TEM image of exfoliated MoS₂ monolayers. **d**, Pd₃P₂S₈ nanodots fabricated via electrochemical Li⁺ intercalation-based exfoliation. Left: TEM image of exfoliated Pd₃P₂S₈ nanodots, where the inset

shows a morphology sketch of Pd₃P₂S₈ nanodot denoting the diameter (*D*) and height (*H*). Middle: statistical size analysis of Pd₃P₂S₈ nanodots, as extracted from the TEM data (mean size: 2.3 nm; standard deviation: 0.6 nm). Right: statistical height analysis of Pd₃P₂S₈ nanodots measured using an atomic force microscope (mean thickness: 1.1 nm; standard deviation: 0.4 nm). **e**, Galvanostatic discharge curve of a Li⁺/layered material (Li_xLM) half-cell. By controlling the cutoff voltage, the amount of Li⁺ intercalation can be regulated so that intercalation can stop at the desired level. **f**, Schematic illustration of a columnar cell (left), coin cell (middle) and soft-pack battery (right) for electrochemical Li⁺ intercalation-based exfoliation. For the detailed composition and structure, as well as the assembly and disassembly process for these electrochemical cells, readers are referred to refs. ^{8,34,36}. Panels adapted with permission from: **a**, ref. ¹², American Chemical Society; **b**, ref. ³², Springer Nature Ltd; **c**, **e**, ref. ⁸, Springer Nature Ltd; **d**, ref. ³⁵, Springer Nature Ltd; **f** (left), ref. ³⁴, Wiley.

(Fig. 4g)⁶⁸. The intercalation process involves the formation of coordination bonding between 4,4'-dipyridyl disulfide and the metal nodes. Exfoliation is induced by selective cleavage of the disulfide bond (equation (26), Table 1) using trimethylphosphine. This fabrication route can proceed efficiently under mild conditions (ambient conditions) and can achieve a ~90% overall yield of 2D MOF flakes with a thickness of <1.2 nm, higher than the yields provided by the direct liquid-exfoliation strategy (normally <15%)⁶⁹.

Alkylamines

Alkylamines (for example, propylamine, butylamine and hexylamine) can also be used as molecular intercalants to enlarge the interlayer spacing of layered materials, facilitating delamination following intercalation¹⁰. The space expansion of layered materials via alkylamine intercalation is dependent on the length of the alkylamine chain. Longer alkylamine chains result in larger expansion between the layers, and therefore brings a more positive promotion to delamination. However,



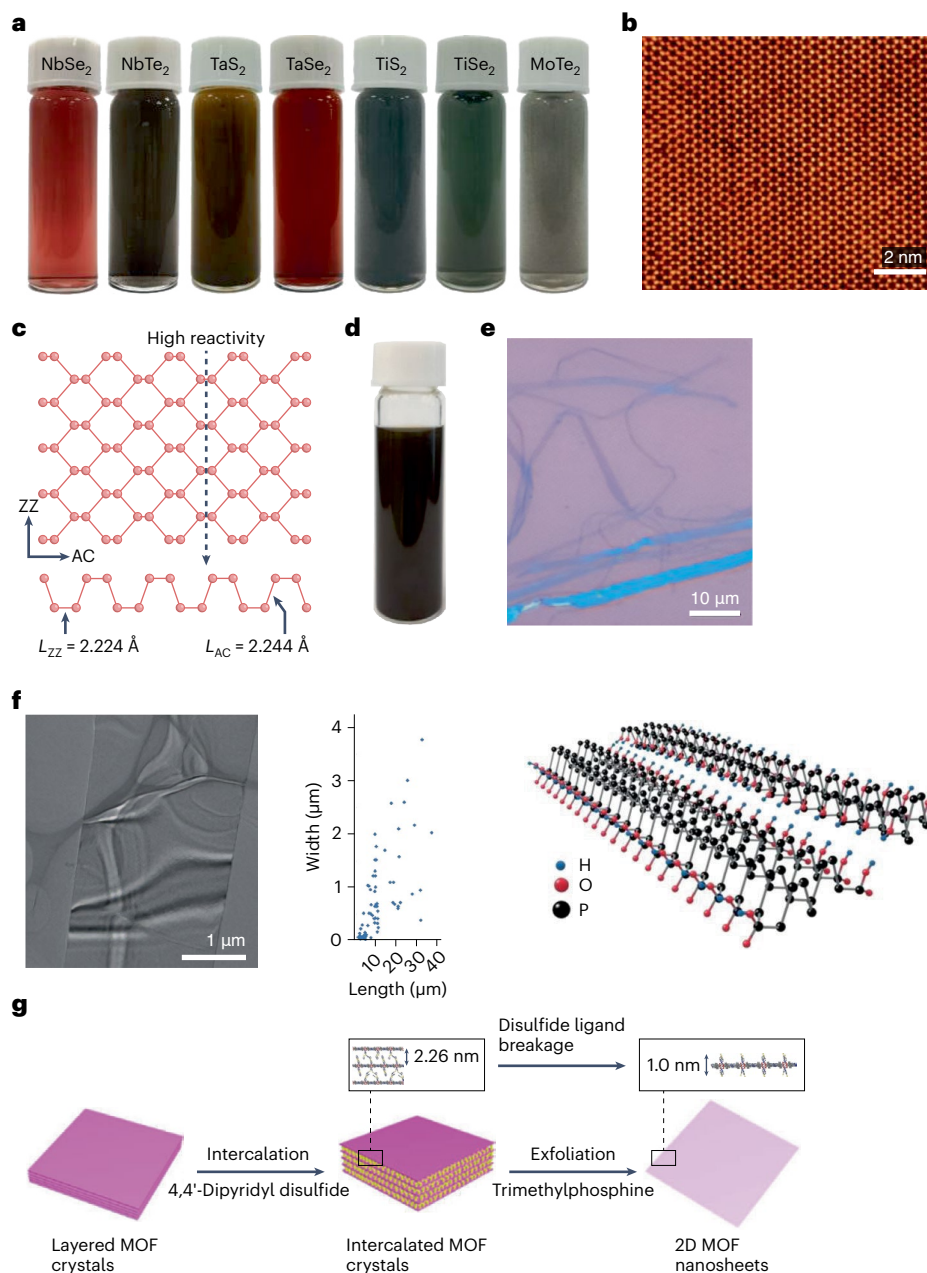


Fig. 4 | R_4N^+ ion, anion and molecular intercalation-based exfoliation.

a, Photographs of electrochemical TBA^+ intercalation-based exfoliated TMD nanosheets dispersed in propylene carbonate solvent. **b**, Atomic-resolution scanning tunnelling electron microscopy–annular dark field image of $NbSe_2$ monolayer prepared via TPA^+ intercalation-based exfoliation, revealing a nearly perfect atomic lattice with a low defect density. **c**, Anisotropic structure of phosphorene. The ZZ direction is more reactive due to a longer P–P bond. **d**, Digital photograph of a BP nanoribbon dispersion in propylene carbonate solvent. **e**, Optical microscope image of BP nanoribbons prepared using

TPA^+ intercalation-based exfoliation. **f**, BP nanoribbons fabricated via electrochemical BF_4^- intercalation-based exfoliation. Left: TEM image of exfoliated BP nanoribbons. Middle: length versus width scatterplot of BP nanoribbons, as extracted from the TEM data. Right: crystal structure of exfoliated BP nanoribbons. **g**, Schematic illustration of molecular intercalation-based exfoliation (using 4,4'-dipyridyl disulfide) for the production of MOF nanosheets. Panels adapted with permission from: **a, b**, ref. ⁴², Springer Nature Ltd; **c–e**, ref. ⁴³, Wiley; **f**, ref. ¹⁹ under a Creative Commons licence [CC BY 4.0](https://creativecommons.org/licenses/by/4.0/); **g**, ref. ⁶⁸, American Chemical Society.

when the molecular length is larger than the interlayer distance (for instance, the length of hexylamine (7.7 Å) is larger than the interlayer distance of TiS_2 (5.7 Å)¹⁰), intercalation resistance will increase, which makes the insertion difficult. Interestingly, a tandem intercalation strategy based on a short ‘initiator’ molecule (propylamine) and a long ‘primary’ molecule (hexylamine) can solve this problem¹⁰. Using short initiator molecules to open up the interlayer gap followed by the insertion of long primary molecules, intercalation can be completed in a short time (~10 h). TiS_2 , ZrS_2 , NbS_2 and MoS_2 monolayers have been successfully exfoliated from their colloidal layered counterparts using this tandem

intercalation-based exfoliation method¹⁰. The strength of this strategy also lies in the safe and mild room-temperature operating conditions, with no gas (for example, hydrogen, sulfur dioxide) being generated.

Factors influencing the quality of exfoliated nanosheets

Properties of the starting bulk crystal

The intrinsic properties (for example, the crystal phase or elemental composition) of the starting crystal can influence the quality of the resulting nanosheets. Taking Li^+ intercalation-based exfoliation as

an example, using 2H-MoS₂ as the starting material, MoS₂ monolayers with mixed phases (2H and 1T/1T') are typically obtained^{12,70} due to the incomplete phase transition from 2H to 1T/1T'. By contrast, when 1T'-MoS₂ is used as the starting material, 1T'-MoS₂ monolayers of high phase purity (over 97%) can be obtained due to the avoidance of phase transition²⁷.

The phases of the starting crystals can also influence the lateral size of the Li⁺ intercalation-based exfoliated nanosheets (Fig. 5a); for example, a 2H-MoS₂ starting crystal yields monolayer counterparts with a lateral size of ~1.0 μm (refs. 12,27) and a 1T'-MoS₂ starting crystal yields monolayer counterparts with a lateral size of tens of micrometres²⁷. This is a consequence of the lattice strain difference of the intercalation compounds for these two phases. Theoretical calculations have confirmed that a higher compressive stress occurs in Li⁺/2H-MoS₂ compounds (1.423 GPa) than in Li⁺/1T'-MoS₂ compounds (0.011 GPa)²⁷. A large compressive stress leads to in-plane wrinkles (Fig. 5b) and results in in-plane fracture during the subsequent exfoliation process using gentle manual shaking, forming small-sized final nanosheets²⁷.

The elemental composition of the starting crystal also effects the lattice strain of the intercalation compounds during the Li⁺ intercalation process, thus influencing the lateral size of the final nanosheets. In terms of TMDs (which have the general formula MX₂, where M is a transition metal and X is a chalcogen), theoretical calculations have shown that the difference value of the lattice parameter *a* (that is, $\Delta a = a(\text{MX}_2) - a(\text{LiMX}_2)$) increases with the metal atom along each row of the periodic table and decreases down each column²⁶ (Supplementary Fig. 3). Large values of Δa imply large lattice strains, which then lead to large in-plane wrinkles and, ultimately, small nanosheet sizes. Therefore, the lateral size of the final nanosheets displays a diametrically opposite trend with Δa (ref. 26) (Fig. 5c).

Intercalant

As stated above, a wide variety of intercalants can be used for intercalation-based exfoliation. Different intercalants result in different product qualities. For example, the Li⁺ intercalant is better for the production of MoS₂ monolayers with a high proportion of the 1T phase^{12,33}, whereas the R₄N⁺ intercalant is better for obtaining high-purity 2H-phase MoS₂ nanosheets⁶. This is because inserting Li⁺ into MoS₂ causes a phase transition from 2H to 1T, but the insertion of R₄N⁺ avoids such a phase transition⁶. For graphene, when BF₄⁻ is used as an intercalant, the electrochemically exfoliated graphene is accompanied by fluorine functionalization⁵¹, facilitating improvements in the thermal stability and transparency of graphene. When using an SO₄²⁻ intercalant, the electrochemically exfoliated graphene will be partially oxidized, forming some oxygen-containing functional groups (for instance, hydroxyl) on the surface⁵⁸. These functional groups can act as catalytic sites, contributing to an improved catalytic performance of the exfoliated graphene. Alternatively, electrochemical R₄N⁺ intercalation-based exfoliation typically yields graphene with minimal defects due to its non-oxidative production route⁴⁴.

Beyond the identity of the intercalant, its concentration is also a crucial factor. An experimental study²⁴ has proved that by controlling *x* to be <0.2 (*x* = Li/Mo in Li_{*x*}MoS₂), the exfoliated MoS₂ nanosheets maintain their original 2H phase, whereas when *x* is >2, a phase transition from 2H to 1T/1T' occurs. In addition, the *x* value also affects the thickness distribution of the final nanosheets. This study²⁴ demonstrated that by maintaining *x* = 0.1, trilayer MoS₂ nanosheets are preferentially yielded. This can be explained using the theory of staging intercalation²⁴ (Fig. 5d) in which intercalation can occur between each layer (a stage-1 intercalation compound), every two layers (a stage-2 intercalation compound), every three layers (a stage-3 intercalation compound) and so on. After exfoliation, these preferentially yield the corresponding monolayer, bilayer or trilayer nanosheets. DFT calculations have shown that when *x* = 0.1, the preferential intercalation stage is 3, leading to the nanosheets being trilayers.

Solvent

A suitable solvent plays a key role in the intercalation, exfoliation and subsequent processing of the layered materials and their atomically thin counterparts. Key properties of the solvent which can affect the product quality are its polarity, surface energy (surface tension) and Brønsted–Lowry acidity.

The polarity of the solvent affects the efficiency of intercalation via determining the dissolution or solvation of the intercalants. These dissolved or solvated intercalants are the real intercalation species (guest) and play a decisive role in the intercalation efficiency⁴⁷. The judicious choice of solvent with a suitable polarity can maximize the intercalation and subsequent exfoliation efficiency. For example, BP can be electrochemically exfoliated using alkylammonium-cation intercalation in polar solvents (such as dimethyl sulfoxide, propylene carbonate, *N*-methylpyrrolidone, *N,N*-dimethylformamide, pyrrolidine dithiocarbamate and acetonitrile), whereas non-polar solvents (for example, toluene and dichloromethane) do not yield the exfoliated BP nanosheets⁴⁷. This was attributed to the better solubility of the alkylammonium cations in polar solvents, which promotes the easy formation of solvated cations for high intercalation and exfoliation efficiencies⁴⁷.

The surface energy (or surface tension) of the solvent is also critical for exfoliation. Earlier studies have suggested that the closer the surface energy of the solvent and layered material, the easier the exfoliation, whether for direct liquid-phase exfoliation^{4,5,71} or intercalation-based exfoliation⁴⁷. The surface energy of layered materials refers to the energy per unit area that is needed to overcome the interlayer van der Waals forces when cleaving two atomic layers⁷¹. The surface energy of the liquid solvent is calculated from its surface tension^{5,71}.

As stated previously, the Brønsted–Lowry acidity (or hydrogen-bonding component) of the solvent has a significant influence on the exfoliation mechanism. Protic solvents typically result in bubble release, which plays a strong role in the exfoliation mechanism^{11,12}. Aprotic solvents facilitate the dispersion and isolation of atomic layers by coordinating the charged layers and ions^{13,14}.

Applied voltage or current

For electrochemical intercalation-based exfoliation strategies, the magnitude and duration of the applied voltage are key factors that affect the qualities of the final nanosheets. Typically, increasing the applied voltage within a certain range and prolonging the time can help to achieve full intercalation, therefore improving the monolayer yield of the final products^{45,52} (Fig. 5e). However, applying too high a voltage or increasing time too much may lead to excessive reduction or oxidation, with the risk of crystal decomposition. In addition, the applied current density will affect the morphology of the final products¹⁹. Taking the electrochemical BF₄⁻ intercalation-based exfoliation method as an example, with the continuous increase in current density from <0.1 to 0.2–0.3 A cm⁻² and then to 0.5 A cm⁻², the morphology of the final BP products evolves from nanosheets to nanobelts and then to quantum dots, respectively¹⁹.

Exfoliation

The exfoliation method after intercalation isolates the atomic layers directly. The lateral size of the isolated atomic layers is affected by the exfoliation power. Theoretically, the higher the power, the greater the fragmentation of the atomic layers, and thereby the smaller the lateral size of the resulting nanosheets. Exfoliation by gentle manual shaking (low power) can prevent in-plane destruction and retain the integrity of the in-plane layers, thereby maximizing the sizes of the resulting nanosheets (Fig. 5f, top)²⁶. By contrast, exfoliation via a sonication method (high power) may cause in-plane fragmentation of the layers, miniaturizing the resulting nanosheets (Fig. 5f, bottom)^{12,20,33}. Experimental studies have demonstrated that the size of the Li⁺ intercalation-based exfoliated nanosheets via shaking exfoliation can reach tens of

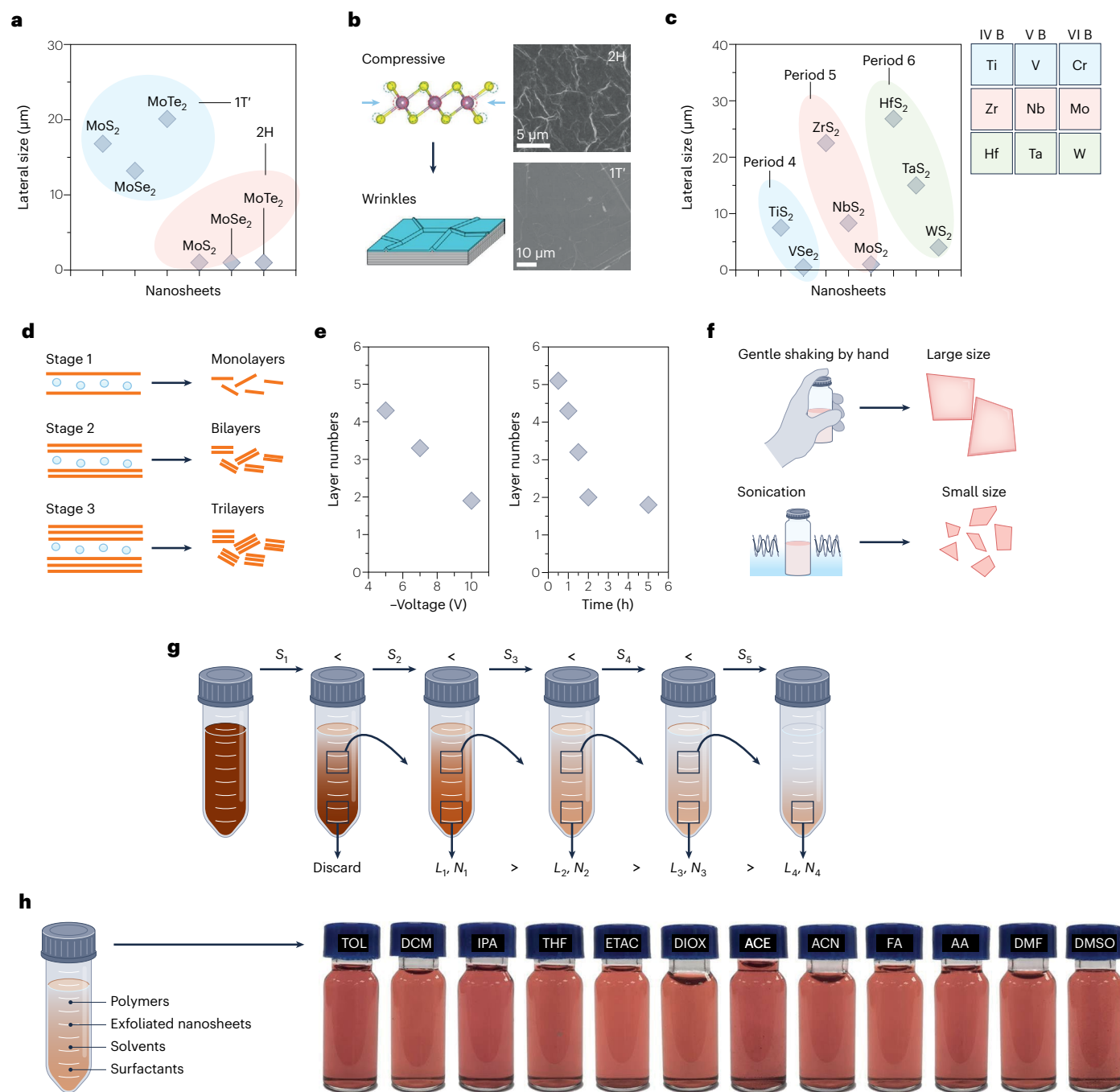


Fig. 5 | Factors influencing the qualities of exfoliated nanosheets. a, Average lateral size of exfoliated MoS_2 (as well as MoSe_2 and MoTe_2) monolayers with the distorted octahedral (1T') and the hexagonal (2H) phase as the starting materials. Data points are from ref. ²⁷. **b**, Compressive stress and the induced in-plane wrinkles in Li_xMoS_2 . Left: schematic illustration of the compressive stress and in-plane wrinkles. Atom colour code: S, yellow; Mo, purple. The dotted blue and red lines indicate the positions after compression of the S and Mo atoms, respectively. Right: SEM images of 2H- MoS_2 and 1T'- MoS_2 crystals after Li^+ intercalation. The surface of 2H- MoS_2 shows dense in-plane wrinkles after intercalation, whereas the surface of 1T'- MoS_2 shows sparse in-plane wrinkles after intercalation. **c**, Periodic lateral size distribution of TMD nanosheets produced via the Li^+ intercalation-based exfoliation strategy. Data points are from ref. ²⁶. **d**, Staging intercalation and exfoliation. **e**, Average layer numbers of exfoliated AgCrS_2 nanosheets with different magnitudes (left) and durations (right) of the applied voltage. Data points are from ref. ⁵².

f, Schematic illustration of exfoliation by gentle manual shaking (top) and via sonication (bottom). **g**, Liquid-cascade centrifugation treatment. The average lateral size (L) and the layer number (N) of the final collected nanosheets decrease with a successive increase in the centrifugal speed (S). **h**, Printable ink, which contains size-selected nanosheets, solvents, polymeric binders and/or surfactants. The vials show an ink example, which is the ink of exfoliated NbSe_2 nanosheets in different solvents, the full names, molecular formulae, structural formulae and polarity indices of which are displayed in Supplementary Table 5. TOL, toluene; DCM, dichloromethane; IPA, isopropyl alcohol; THF, tetrahydrofuran; ETAC, ethyl acetate; DIOX, 1,4-dioxane; ACE, acetone; ACN, acetonitrile; FA, formic acid; AA, acetic acid; DMF, *N,N*-dimethylformamide; DMSO, dimethyl sulfoxide. Panels adapted with permission from: **b** (left), ref. ²⁶, American Chemical Society; **b** (right), ref. ²⁷, Wiley; **h**, ref. ⁴², Springer Nature Ltd. The design concept of **g** is derived from ref. ⁹.

micrometres²⁶, and generally less than 1.0 μm when using sonication exfoliation ($\sim 100\text{ W}$)^{12,20,33}.

Centrifugation

Post-exfoliation, a centrifugation step for the purification and collection of the atomically thin sheets is crucial. Hydrodynamic forcing (centrifugal speed) is a core factor in this step. Typically, low-speed centrifugation (such as 2,000 revolutions per min) is performed to remove large particles, followed by high-speed centrifugation (for instance, 10,000 revolutions per min) to release the intercalant, as shown in Fig. 2d. Intercalation-based exfoliated flakes are always polydisperse, with a lateral size ranging from tens of nanometres to hundreds of micrometres and a thickness of a single layer to several layers. Size selection for such widely distributed nanosheets can be carried out via liquid-cascade centrifugation treatment (Fig. 5g) to narrow the distributions in both lateral size and thickness^{9,24}. The resulting size-selected nanosheets are ideal building blocks for the manufacture of certain electronic, photonic and optoelectronic devices^{42,56}. It is of note that, for good compatibility with printing techniques, redispersion of the size-selected nanosheets into water or other solvent to form a printable ink (Fig. 5h) is required. During this step, rheological refinement through the addition of polymeric binders and/or surfactants to the ink is essential to ensure that the ink matches well with the deposition technology and substrate. For a detailed description of the ink formulation, the reader is referred to the recent review of Pinilla and co-workers³.

Phase transition

The intercalation-based exfoliation strategy is a generally scalable method for the fabrication of atomically thin flakes, but the resultant nanosheets may undergo a phase transition during the intercalation and exfoliation steps, therefore differing structurally and electronically from their bulk counterparts^{72,73}. Previous experimental studies^{12,33} and theoretical investigations⁷³ have suggested that such a phase transition is more likely to occur in TMD nanomaterials. TMDs have structural polymorphs with different in-plane bonding configurations. These bonding configurations are close in energy because of the relatively small electronegativity of the chalcogen elements (S, Se and Te), leading to the facile occurrence of phase transitions under near-ambient conditions⁷³.

Structural phases of TMDs

TMDs, with the general formula MX_2 , have three well-known polytypic structures which result from the different coordination geometries of the transition metal atoms⁷². These are the 2H, 1T and 1T' phases, which exhibit the trigonal prismatic, octahedral and distorted octahedral coordination structure, respectively, for the metal atoms (Fig. 6a). These structural phases also exhibit distinct stacking orders of the three atomic planes (X–M–X). The most studied 2H phase corresponds to the Bernal (ABA) stacking, whereas the stacking order of the atomic planes in the 1T phase is rhombohedral ABC. This diversity of structural phases gives rise to various electronic properties. For example, 2H-MoS₂ exhibits semiconducting properties with an optical bandgap in the range of 1.0–2.5 eV (ref. ⁷⁴). By contrast, 1T- and 1T'-MoS₂ show metallic and semimetallic character, respectively⁷⁵.

Phase transition

During the intercalation-based exfoliation process (especially when Li-based intercalants are used), the intercalation of cations involves the simultaneous injection of electrons into the *d* orbitals of the host transition metal atoms⁷³ to maintain overall charge neutrality. The injection of electrons beyond a certain threshold causes the stability of the 2H phase to be lower than that of the 1T or 1T' phase, inducing the corresponding in-plane phase transitions (Fig. 6b). For an explanation of this phenomenon the reader is referred to specific articles on crystal field theory^{73,76,77}. Experimentally, the occurrence of phase transitions

(from 2H to 1T or 1T') has been probed using scanning transmission electron microscopy (STEM), XPS, Raman spectroscopy, X-ray diffraction and photoluminescence. Among them, STEM offers an opportunity to distinguish the detailed structures of the 2H, 1T and 1T' phases⁷⁰. The deconvolution of high-resolution XPS peaks provides the feasibility for the quantitative analysis of the mixed phases⁷⁸.

Phase restoration

Previous theoretical studies have suggested that the 1T phase is metastable and can be transformed back into the thermodynamically stable 2H phase (Fig. 6c)^{12,79}. Eda et al. experimentally demonstrated the restoration of the original 2H-phase MoS₂ from the 1T/1T' phases through mild annealing (above 300 °C, 1 h) using a hot plate in an argon-filled glovebox¹². XPS and Raman analyses indicated that the extent of the restored original 2H phase gradually increases with an increase in the annealing temperature. The fraction of the 2H phase reaches 95% at 300 °C. In addition, recent studies have suggested the possibility of the restoration of the 2H-phase MoS₂ via hydrothermal treatment under a nitrogen atmosphere at -200 °C (ref. ⁸⁰) or via infrared laser-induced processing⁸¹.

High-purity phase preparation

Previous electrostatic gating studies have suggested that the 2H-to-1T phase transition happens only when the electron injection exceeds a certain threshold^{82,83}; for MoS₂, this threshold is 0.29 electrons per formula unit⁶. Therefore, reducing the electron injection was recently proposed as a theoretical method^{6,82–84} for preventing phase transitions during intercalation-based exfoliation. Lin and co-workers⁶ suggested that using larger cations (for example, THA⁺) as the intercalant during the process of electrochemical intercalation-based exfoliation may reduce the electron injection (Fig. 6d). The large size of THA⁺ (Fig. 6e) naturally limits the injected number of ions into the interlayer of the TMD and thus reduces the number of electrons injected⁶. The properties of the obtained high-purity semiconducting 2H-phase MoS₂ nanosheets were confirmed via their Raman (Fig. 6f), ultraviolet-visible absorption (Fig. 6g,h), XPS (Fig. 6i) and photoluminescence (Fig. 6j) spectra, demonstrating the experimental feasibility of this method.

Applications of exfoliated nanosheets

When layered materials are exfoliated into atomically thin layers, unique properties are unlocked^{3,85}. For example, graphene shows outstanding electric conductivity and mechanical strength compared with its bulk counterpart graphite⁸⁶. The MoS₂ monolayer is semiconducting with a direct bandgap of 1.8 eV, exhibiting unique physical, optical and electrical properties (for example, a unique quantum luminescence efficiency¹²) compared with the bulk MoS₂ crystal, which is an indirect bandgap semiconductor with a bandgap of 1.2 eV.

Crucially, intercalation-based exfoliated nanosheets are compatible with solution-based deposition techniques (such as dropcasting, spincoating, inkjet printing, industrial roll-to-roll coating and vacuum filtration)^{3,9,87,88}. This enables easy and scalable manufacture of various customizable devices, via the deposition of exfoliated nanosheets on various substrates (for example, SiO₂/Si (refs. ^{6,42}), rigid glass²² or porous polymer^{25,89}), if necessary, followed by a lithographic process involving standard photolithography, dry or wet etching, and metal (such as gold or titanium) deposition^{6,90}.

Exfoliated atomically thin sheets (for example, graphene, TMDs, BP, h-BN, MOF and Sb) can therefore be used as the building blocks of modern devices, leading to a range of applications in the fields of electronics, photonics, optoelectronics, energy storage, environmental remediation, bioengineering and beyond³ (Supplementary Table 2). Here we highlight several notable application examples.

Exfoliated graphene is interesting for various electronic devices (for instance, field-effect transistors)^{57,58} and energy devices (such as supercapacitors)^{16,59} due to its high electrical mobility (up to

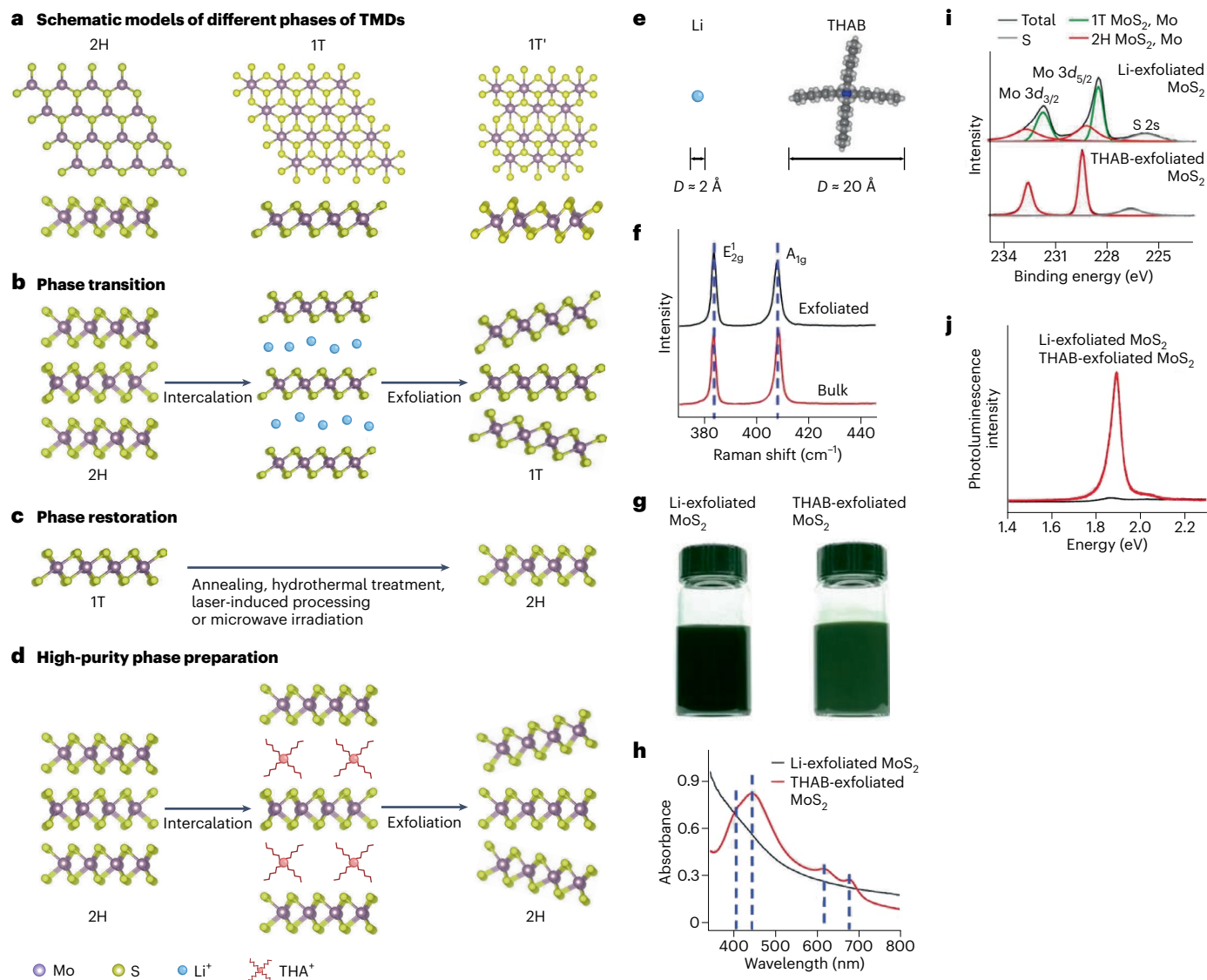


Fig. 6 | Phase transitions during the intercalation-based exfoliation process. **a**, Schematic models of the different TMD phases, including the 2H, 1T and 1T' phases. Top: top view showing the typical atomic arrangement of a single layer. Bottom: side view showing the typical packing sequence. **b**, Schematic illustration of phase transformation during the Li⁺ intercalation-based exfoliation process. **c**, Schematic illustration of phase restoration via annealing, hydrothermal treatment, laser-induced processing or microwave irradiation. **d**, Schematic illustration of high-purity 2H-phase MoS₂ preparation via electrochemical THA⁺ intercalation-based exfoliation. **e**, Schematic models of tetraheptylammonium bromide (THAB) and lithium (Li) showing the size difference between the intercalants. **f**, Raman spectra of THA⁺-exfoliated MoS₂ nanosheets and the bulk MoS₂ sample. Both Raman peaks in the bulk and exfoliated MoS₂ sample belong to 2H-phase MoS₂ (ref. ¹¹²). **g**, Photograph of the dispersion of Li⁺-exfoliated MoS₂ nanosheets in water and THA⁺-exfoliated

MoS₂ nanosheets in isopropyl alcohol. The black colour of the suspension of Li⁺-exfoliated MoS₂ nanosheets shows the non-selective absorption of light in the visible range, indicating the metallic nature of the Li⁺-exfoliated MoS₂ nanosheets. By contrast, the suspension of THA⁺-exfoliated MoS₂ nanosheets appears green, suggesting the partial absorption of light in the visible range and the semiconducting nature of the THA⁺-exfoliated MoS₂ nanosheets¹². **h**, Ultraviolet–visible absorption spectra of THA⁺-exfoliated MoS₂ and Li⁺-exfoliated MoS₂. **i**, XPS spectra of THA⁺-exfoliated MoS₂ nanosheets and Li⁺-exfoliated MoS₂ nanosheets, which indicate the pure 2H phase for the THA⁺-exfoliated nanosheets and the mostly the 1T phase for the Li⁺-exfoliated nanosheets⁷⁸. The green, red, grey and black curves denote Mo in 1T-phase MoS₂, Mo in 2H-phase MoS₂, S and the overall signal, respectively. **j**, Photoluminescence spectra of THA⁺-exfoliated MoS₂ nanosheets and Li⁺-exfoliated MoS₂ nanosheets. Panels **e–j** reproduced with permission from ref. ⁶, Springer Nature Ltd.

$2.5 \times 10^5 \text{ cm}^2 \text{ V}^{-1} \text{ s}^{-1}$, theoretically) at room and cryogenic temperatures. However, many functional devices would also benefit from properties beyond the capabilities of graphene. For instance, the broadband nonlinear optical response feature of exfoliated atomically thin Sb nanosheets (which have a large nonlinear refractive index of $-10^{-5} \text{ cm}^2 \text{ W}^{-1}$) enables their applications in nonlinear photonic devices (such as optical switchers, Kerr shutters and beam shapers)³⁷. Exfoliated In₂Se₃ flakes have strong, wide-range responsivity from the ultraviolet to near-infrared absorption regions, showing their potential for

optoelectronic devices (such as photodetectors)⁵⁰. The high theoretical specific capacity of exfoliated BP flakes enables them to be used as electrode materials for battery applications (in terms of sodium-ion batteries, the theoretical specific capacity is up to $2,596 \text{ mAh g}^{-1}$)⁴⁵. Exfoliated MoS₂ monolayers have a high fluorescence quenching ability and different affinities for single-stranded DNA (deoxyribonucleic acid) and double-stranded DNA, therefore they show potential as biosensors⁹¹. Exfoliated 1T' MoTe₂ is a type-II Weyl semimetal, showing potential as a saturable absorber for ultrafast photonics in all-fibre mode-locked

lasers⁵⁶. High-purity semiconductor 2H-phase MoS₂ materials prepared via THA⁺ intercalation-based exfoliation enable the creation of high-performance thin-film transistors (room-temperature mobilities: 10 cm² V⁻¹ s⁻¹; on/off ratios: 10⁶) and more complex electronic devices, such as logic gates and computing circuits⁶.

Films (with an adjustable thickness of 1.5–24.0 μm) generated by ordered stacking of exfoliated 1T-MoS₂ quantum sheets (~6.1 nm in lateral size) have narrow and ultrashort (~1.2 nm and ~6.1 nm, respectively) hydrophobic nanochannels, giving them an ultrafast ion-transport ability. Such films, as structural units of an electrode, give the corresponding capacitor an outstanding energy-storage performance (with a volumetric capacitance of 437 F cm⁻³ tested at 2,000 mV s⁻¹)³⁶. Membranes produced by restacking exfoliated and covalently functionalized MoS₂ nanosheets hold channel widths that can be tuned by covalent functional groups. Such membranes, as a core component of nanofiltration and desalination devices, show excellent rejection rates toward various dyes (>90%) and sodium chloride (>80%)^{25,89}. Van der Waals thin films (of ~30 nm thickness) consisting of staggered semiconducting MoS₂ nanosheets (produced via THA⁺ intercalation-based exfoliation) feature bond-free van der Waals interfaces among the staggered MoS₂ flakes⁹⁰. Such a bond-free nature endows the van der Waals thin films with high degrees of freedom in their free sliding and rotation abilities, ensuring their mechanical malleability⁹⁰. In addition, the fine percolating networks of nanochannels in these thin films provide permeability and breathability⁹⁰. Such films show great application potential in flexible bioelectronic devices, such as in leaf-gate and skin-gate transistors⁹⁰.

The atomically thin nature of exfoliated nanosheets also makes them advantages for a variety of catalytic applications over their bulk crystal counterparts^{20,21,29,35,38,68,92–95} (Supplementary Table 3). These superiorities include quantum confinement, short transmission distances of the carriers, large surface-area-to-volume ratios, rich low-coordinated surface atoms, among others. For photocatalytic applications, the quantum confinement effect endows atomically thin semiconducting nanosheets with tunable band structures⁹⁶. The short transmission distance of carriers from the interior of the material to its surface suppresses the bulk recombination of charge carriers⁹². A large surface-area-to-volume ratio enables rich point contact between the reactants and catalytic sites; this is also an advantage for light capturing. Rich low-coordinated surface atoms offer abundant adsorption and activation sites for typical reactant molecules. All these features contribute to an outstanding photocatalytic performance of exfoliated atomically thin semiconductors^{68,92,94,95}. Beyond photocatalysis, exfoliated nanosheets also exhibit superiority over bulk materials for electrocatalysis. For example, exfoliated monolayers of metallic 1T-phase TMDs (such as WS₂ (ref. 20), MoS₂ (refs. 21,29) and PtTe₂ (ref. 97)) show an enhanced electrocatalytic performance for the HER, owing to their high conductivity, low-loss electrical transport and rich catalytically active sites. Exfoliated Sb thin layers have a large number of catalytically active edge sites, unlocking their electrocatalytic activity for CO₂ reduction³⁸. Exfoliated Pd₃P₂S₈ ultrasmall nanosheets have an amorphous structure, which is different from their bulk crystal counterpart. Such miniaturization and amorphization means that, unlike the inert bulk crystal, the ultrasmall nanosheets can be active electrocatalysts for the HER³⁵.

Intercalation-based exfoliation typically yields thin, large-area flakes. Such products are good building blocks for large-area thin-film devices⁴⁹. These devices are difficult to manufacture using direct liquid-exfoliated nanosheets, whose lateral size is normally below 1.0 μm. In addition, intercalation-based exfoliation often introduces basal-plane defects to the final products. Such defects do not usually occur in direct liquid-exfoliated nanosheets. Although defects may be undesirable in certain applications, they are beneficial for catalysis⁹⁴. Besides, intercalation-based exfoliation may induce phase transitions (2H to 1T/1T'); therefore, it can be used as a phase-engineering tool for

various applications, such as low-resistance contact transistors⁷⁸. These applications can benefit explicitly from intercalation-based exfoliation methods over standard direct liquid exfoliation.

Outlook

Intercalation-based exfoliation strategies point to a productive future for the synthesis of atomically thin sheets. However, challenges remain.

Perfecting the strategies

Several intercalation-based exfoliation methodologies have been established with their own merits and have been introduced in this Review; however, no method is perfect. These imperfections relate to the product quality (including yield, structural integrity, controllability, uniformity, stability and repeatability) and the operating conditions of the method, such as time, temperature, safety and complexity.

For example, Li⁺ intercalation-based exfoliation involves interesting TMD phase transitions (2H to 1T)^{8,12,33}, but the degree of phase transition and the proportion of the two phases in the final product cannot be accurately controlled. R₄N⁺ intercalation-based exfoliation provides a means for the production of large domain-sized sheets (of up to hundreds of micrometres)^{42,49}, stimulating their application potential for large-area thin-film devices. However, the uniformity of these sheets is poor, with sizes ranging from just a few to hundreds of micrometres. SO₄²⁻ or BF₄⁻ intercalation-based exfoliation strategies tend to yield oxidized¹⁶ or fluorinated⁶¹ graphene, which improves the catalytic activity or thermal stability and transparency, but there is a lack of control over the degree of oxidation and fluorination. High-quality BP nanoribbons can be effectively produced via intercalation-based exfoliation using Li⁺ (with a lithium metal intercalant)³² or BF₄⁻ (ref. 19), but these methods are limited by, respectively, the complexity of the operation and the defects of the product structure (where the edges are usually oxidized).

Additional research into these intercalation-based exfoliation strategies should be carried out to optimize the strategies in terms of product quality and operating conditions, ultimately improving their applications.

Universalizing the strategies

Many atomically thin materials can now be produced using intercalation-based exfoliation techniques. What started with the production of graphene^{16,44,46,53,57–59}, TMDs^{6,10,12,17,20,24,26,27,29–31,33,34,36,42,54–56,97}, h-BN³⁴, BP^{19,32,40,43,45,47,49} and A₂B₃ (such as In₂Se₃)^{6,34,50,51,67} has now evolved to produce atomically thin MOFs^{68,93}, Sb (refs. 37,38), AMX₂ (for instance, AgCrS₂)⁵², Pd₃P₂S₈ (ref. 35), PdSeO₃ (ref. 41), Bi₁₂O₁₇Cl₂ (ref. 92), BiOCl (ref. 95), ZnIn₂S₄ (ref. 94), Ni₃Cr₂P₂S₉ (ref. 98) and beyond. There are more than 5,600 experimentally known layered materials⁹⁹, and the material exfoliated at present is only the tip of the iceberg for the huge library of layered materials.

Universalizing intercalation-based exfoliation strategies to exfoliate more layered materials, mass-produce atomically thin nanomaterials and explore emerging applications based on their outstanding material properties is in line with a key developmental direction of materials science and engineering—that is, developing new materials.

To promote the generalization of the intercalation-based exfoliation strategy, the properties of the layered materials must be matched to the intercalation and exfoliation processes. The appropriate intercalant, solvent, intercalation conditions (for example, time, atmosphere and applied voltage), exfoliation mode and power must be selected for the intercalation-based exfoliation synthesis of emerging atomically thin nanomaterials. Traditionally, a large number of experiments are needed to select the appropriate synthetic variables. This is time-consuming and labour-intensive. High-throughput computational calculations may provide a fast track for these explorations⁹⁹. Data-driven screening should become an integral part of the synthetic toolkit

in future research¹⁰⁰, which will help to universalize the intercalation-based exfoliation strategy.

Understanding the mechanisms

Understanding the mechanisms (which include phase transition, phase restoration, high-purity phase preparation, defect formation, oxidation functionalization, fluorination functionalization and property evolution) that are involved in the intercalation and exfoliation processes should be emphasized. This is important as it can facilitate the rational design of future experiments, such as the on-demand synthesis of 2D nanosheets with special properties (for instance, defect-rich or defect-free flakes). State-of-the-art in situ imaging, spectroscopy and electrochemical characterization methods offer a powerful tools for exploring these mechanisms in real time^{101–105}. For instance, in situ liquid-cell TEM^{101–103} can monitor the phase transition as it occurs during the intercalation and exfoliation processes. In situ Raman spectroscopy provides a feasible means of tracking the evolution of the electronic and optical properties of layered materials during the intercalation and exfoliation process¹⁰⁴. In situ optical microscopy is an effective tool for directly monitoring the evolution of the material thickness¹⁰⁵.

Modern characterization toolkits are constantly being enriched (as with the advent of X-ray absorption spectroscopy, scanning transmission X-ray microscopy and beyond), providing more sophisticated techniques by which these mechanisms can be clarified. Still, we argue that the most challenging aspect is how to build the right measurement platform that meets the requirements of operando characterization (such as the vacuum environment for TEM imaging) as well as the intercalation and exfoliation conditions. Nanoprocessing technology based on lithography provides technical support for the manufacture of these customized platforms.

Transiting from laboratory to market

Despite the tremendous progress made in intercalation-based exfoliation strategies, there is still a long way to go to achieve a laboratory-to-market transition. The first and most common implementation barrier is scaling up.

The current output of a single production unit (a single electrochemical cell, for example) is at the milligram-to-gram scale³⁶. Such an output level cannot meet the demands of the material market, which needs a kilogram-to-tonne scale. The parallel operation of multiple production units, expanding the scale of a single production unit, or implementing both, can achieve large-scale production and a laboratory-to-market transition. However, this step is still at a stage of early development and requires investment for research into the rational design of production units, batch industrial manufacturing, cost control, optimization of the operating parameters, among other factors.

Economically, there are many barriers to scaling up, resulting from the high price of ingredients (for layered crystals in particular; Supplementary Table 4) and the toxicity of certain solvents. Technically, scaling up the production units, whether intercalation or exfoliation, will also encounter some difficulties. For example, after the intercalation and exfoliation processes, purification and size selection via liquid-cascade centrifugation are typically needed, but this is difficult to scale. Solving these economic and technical concerns will make the road to commercialization, from laboratory to market, much smoother.

The market is the driving force of technology commercialization³. Exfoliated atomically thin sheets can be incorporated into various commercial products, resulting in a variety of potential downstream markets for intercalation-based exfoliation technology. The electronic and optoelectronic device markets should be targeted first since, for many atomically thin materials, including graphene, their electronic and optoelectronic device applications are most likely to bring high economic benefits¹⁰⁶.

Opportunities and challenges coexist in this promising field. We anticipate that the intercalation-based exfoliation strategy will become a central tool in nanotechnology for the production of atomically thin 2D materials in the coming decades.

References

1. Novoselov, K. S. et al. Electric field effect in atomically thin carbon films. *Science* **306**, 666–669 (2004).
2. Novoselov, K. S., Mishchenko, A., Carvalho, A. & Castro Neto, A. H. 2D materials and van der Waals heterostructures. *Science* **353**, aac9439 (2016).
3. Pinilla, S., Coelho, J., Li, K., Liu, J. & Nicolosi, V. Two-dimensional material inks. *Nat. Rev. Mater.* **7**, 717–735 (2022).
4. Nicolosi, V., Chhowalla, M., Kanatzidis, M. G., Strano, M. S. & Coleman, J. N. Liquid exfoliation of layered materials. *Science* **340**, 1226419 (2013).
5. Coleman, J. N. et al. Two-dimensional nanosheets produced by liquid exfoliation of layered materials. *Science* **331**, 568–571 (2011).
6. Lin, Z. et al. Solution-processable 2D semiconductors for high-performance large-area electronics. *Nature* **562**, 254–258 (2018).
7. Zhang, H. Ultrathin two-dimensional nanomaterials. *ACS Nano* **9**, 9451–9469 (2015).
8. Yang, R. et al. High-yield production of mono- or few-layer transition metal dichalcogenide nanosheets by an electrochemical lithium ion intercalation-based exfoliation method. *Nat. Protoc.* **17**, 358–377 (2022).
9. Kelly, A. G., O'Suilleabhain, D., Gabbett, C. & Coleman, J. N. The electrical conductivity of solution-processed nanosheet networks. *Nat. Rev. Mater.* **7**, 217–234 (2022).
10. Jeong, S. et al. Tandem intercalation strategy for single-layer nanosheets as an effective alternative to conventional exfoliation processes. *Nat. Commun.* **6**, 5763 (2015).
11. Joensen, P., Frindt, R. F. & Morrison, S. R. Single-layer MoS₂. *Mater. Res. Bull.* **21**, 457–461 (1986).
12. Eda, G. et al. Photoluminescence from chemically exfoliated MoS₂. *Nano Lett.* **11**, 5111–5116 (2011).
13. Vallés, C. et al. Solutions of negatively charged graphene sheets and ribbons. *J. Am. Chem. Soc.* **130**, 15802–15804 (2008).
14. Cullen, P. L. et al. Ionic solutions of two-dimensional materials. *Nat. Chem.* **9**, 244–249 (2017).
15. Kang, Y.-J., Jung, S. C., Choi, J. W. & Han, Y.-K. Important role of functional groups for sodium ion intercalation in expanded graphite. *Chem. Mater.* **27**, 5402–5406 (2015).
16. Parvez, K. et al. Exfoliation of graphite into graphene in aqueous solutions of inorganic salts. *J. Am. Chem. Soc.* **136**, 6083–6091 (2014).
17. Liu, N. et al. Large-area atomically thin MoS₂ nanosheets prepared using electrochemical exfoliation. *ACS Nano* **8**, 6902–6910 (2014).
18. Lu, J. et al. One-pot synthesis of fluorescent carbon nanoribbons, nanoparticles, and graphene by the exfoliation of graphite in ionic liquids. *ACS Nano* **3**, 2367–2375 (2009).
19. Liu, Z. et al. Unzipping of black phosphorus to form zigzag-phosphorene nanobelts. *Nat. Commun.* **11**, 3917 (2020).
20. Voiry, D. et al. Enhanced catalytic activity in strained chemically exfoliated WS₂ nanosheets for hydrogen evolution. *Nat. Mater.* **12**, 850–855 (2013).
21. Lukowski, M. A. et al. Enhanced hydrogen evolution catalysis from chemically exfoliated metallic MoS₂ nanosheets. *J. Am. Chem. Soc.* **135**, 10274–10277 (2013).
22. Acerce, M., Voiry, D. & Chhowalla, M. Metallic 1T phase MoS₂ nanosheets as supercapacitor electrode materials. *Nat. Nanotechnol.* **10**, 313–318 (2015).

23. Voiry, D. et al. Covalent functionalization of monolayered transition metal dichalcogenides by phase engineering. *Nat. Chem.* **7**, 45–49 (2015).
24. Fan, X. et al. Controlled exfoliation of MoS₂ crystals into trilayer nanosheets. *J. Am. Chem. Soc.* **138**, 5143–5149 (2016).
25. Ries, L. et al. Enhanced sieving from exfoliated MoS₂ membranes via covalent functionalization. *Nat. Mater.* **18**, 1112–1117 (2019).
26. Peng, J. et al. Very large-sized transition metal dichalcogenides monolayers from fast exfoliation by manual shaking. *J. Am. Chem. Soc.* **139**, 9019–9025 (2017).
27. Peng, J. et al. High phase purity of large-sized 1T'-MoS₂ monolayers with 2D superconductivity. *Adv. Mater.* **31**, 1900568 (2019).
28. Tsai, H.-L., Heising, J., Schindler, J. L., Kannewurf, C. R. & Kanatzidis, M. G. Exfoliated–restacked phase of WS₂. *Chem. Mater.* **9**, 879–882 (1997).
29. Voiry, D. et al. Conducting MoS₂ nanosheets as catalysts for hydrogen evolution reaction. *Nano Lett.* **13**, 6222–6227 (2013).
30. Zheng, J. et al. High yield exfoliation of two-dimensional chalcogenides using sodium naphthalenide. *Nat. Commun.* **5**, 2995 (2014).
31. Zhu, X. et al. Exfoliation of MoS₂ nanosheets enabled by a redox-potential-matched chemical lithiation reaction. *Nano Lett.* **22**, 2956–2963 (2022).
32. Watts, M. C. et al. Production of phosphorene nanoribbons. *Nature* **568**, 216–220 (2019).
33. Zeng, Z. et al. Single-layer semiconducting nanosheets: high-yield preparation and device fabrication. *Angew. Chem. Int. Ed.* **50**, 11093–11097 (2011).
34. Zeng, Z. et al. An effective method for the fabrication of few-layer-thick inorganic nanosheets. *Angew. Chem. Int. Ed.* **51**, 9052–9056 (2012).
35. Zhang, X. et al. Lithiation-induced amorphization of Pd₃P₂S₈ for highly efficient hydrogen evolution. *Nat. Catal.* **1**, 460–468 (2018).
36. Chen, W. et al. Two-dimensional quantum-sheet films with sub-1.2 nm channels for ultrahigh-rate electrochemical capacitance. *Nat. Nanotechnol.* **17**, 153–158 (2022).
37. Lu, L. et al. Broadband nonlinear optical response in few-layer antimonene and antimonene quantum dots: a promising optical Kerr media with enhanced stability. *Adv. Opt. Mater.* **5**, 1700301 (2017).
38. Li, F. et al. Unlocking the electrocatalytic activity of antimony for CO₂ reduction by two-dimensional engineering of the bulk material. *Angew. Chem. Int. Ed.* **56**, 14718–14722 (2017).
39. García-Dalí, S. et al. Aqueous cathodic exfoliation strategy toward solution-processable and phase-preserved MoS₂ nanosheets for energy storage and catalytic applications. *ACS Appl. Mater. Interfaces* **11**, 36991–37003 (2019).
40. Yang, S. et al. A delamination strategy for thinly layered defect-free high-mobility black phosphorus flakes. *Angew. Chem. Int. Ed.* **57**, 4677–4681 (2018).
41. Zhang, X. et al. Atomically thin PdSeO₃ nanosheets: a promising 2D photocatalyst produced by quaternary ammonium intercalation and exfoliation. *Chem. Commun.* **56**, 5504–5507 (2020).
42. Li, J. et al. Printable two-dimensional superconducting monolayers. *Nat. Mater.* **20**, 181–187 (2021).
43. Yu, W. et al. Facile production of phosphorene nanoribbons towards application in lithium metal battery. *Adv. Mater.* **33**, 2102083 (2021).
44. Cooper, A. J., Wilson, N. R., Kinloch, I. A. & Dryfe, R. A. W. Single stage electrochemical exfoliation method for the production of few-layer graphene via intercalation of tetraalkylammonium cations. *Carbon* **66**, 340–350 (2014).
45. Huang, Z. et al. Layer-tunable phosphorene modulated by the cation insertion rate as a sodium-storage anode. *Adv. Mater.* **29**, 1702372 (2017).
46. Jeon, I., Yoon, B., He, M. & Swager, T. M. Hyperstage graphite: electrochemical synthesis and spontaneous reactive exfoliation. *Adv. Mater.* **30**, 1704538 (2018).
47. Li, J. et al. Ultrafast electrochemical expansion of black phosphorus toward high-yield synthesis of few-layer phosphorene. *Chem. Mater.* **30**, 2742–2749 (2018).
48. Zhang, Y. & Xu, Y. Simultaneous electrochemical dual-electrode exfoliation of graphite toward scalable production of high-quality graphene. *Adv. Funct. Mater.* **29**, 1902171 (2019).
49. Wang, N. et al. Electrochemical delamination of ultralarge few-layer black phosphorus with a hydrogen-free intercalation mechanism. *Adv. Mater.* **33**, 2005815 (2021).
50. Shi, H. et al. Ultrafast electrochemical synthesis of defect-free In₂Se₃ flakes for large-area optoelectronics. *Adv. Mater.* **32**, 1907244 (2020).
51. Lin, Z. et al. High-yield exfoliation of 2D semiconductor monolayers and reassembly of organic/inorganic artificial superlattices. *Chem* **7**, 1887–1902 (2021).
52. Peng, J. et al. Stoichiometric two-dimensional non-van der Waals AgCrS₂ with superionic behaviour at room temperature. *Nat. Chem.* **13**, 1235–1240 (2021).
53. Zhong, Y. L. & Swager, T. M. Enhanced electrochemical expansion of graphite for in situ electrochemical functionalization. *J. Am. Chem. Soc.* **134**, 17896–17899 (2012).
54. Yu, W. et al. Chemically exfoliated VSe₂ monolayers with room-temperature ferromagnetism. *Adv. Mater.* **31**, 1903779 (2019).
55. Yu, W. et al. Domain engineering in ReS₂ by coupling strain during electrochemical exfoliation. *Adv. Funct. Mater.* **30**, 2003057 (2020).
56. Yu, W. et al. High-yield exfoliation of monolayer 1T'-MoTe₂ as saturable absorber for ultrafast photonics. *ACS Nano* **15**, 18448–18457 (2021).
57. Su, C.-Y. et al. High-quality thin graphene films from fast electrochemical exfoliation. *ACS Nano* **5**, 2332–2339 (2011).
58. Parvez, K. et al. Electrochemically exfoliated graphene as solution-processable, highly conductive electrodes for organic electronics. *ACS Nano* **7**, 3598–3606 (2013).
59. Yang, S. et al. Organic radical-assisted electrochemical exfoliation for the scalable production of high-quality graphene. *J. Am. Chem. Soc.* **137**, 13927–13932 (2015).
60. Liu, N. et al. One-step ionic-liquid-assisted electrochemical synthesis of ionic-liquid-functionalized graphene sheets directly from graphite. *Adv. Funct. Mater.* **18**, 1518–1525 (2008).
61. Zhou, F. et al. Electrochemically scalable production of fluorine-modified graphene for flexible and high-energy ionogel-based microsupercapacitors. *J. Am. Chem. Soc.* **140**, 8198–8205 (2018).
62. Ambrosi, A. & Pumera, M. Electrochemically exfoliated graphene and graphene oxide for energy storage and electrochemistry applications. *Chem. Eur. J.* **22**, 153–159 (2016).
63. Liu, J. et al. Improved synthesis of graphene flakes from the multiple electrochemical exfoliation of graphite rod. *Nano Energy* **2**, 377–386 (2013).
64. Rao, K. S., Senthilnathan, J., Liu, Y.-F. & Yoshimura, M. Role of peroxide ions in formation of graphene nanosheets by electrochemical exfoliation of graphite. *Sci. Rep.* **4**, 4237 (2014).
65. Wang, G. et al. Highly efficient and large-scale synthesis of graphene by electrolytic exfoliation. *Carbon* **47**, 3242–3246 (2009).
66. Ambrosi, A., Sofer, Z. & Pumera, M. Electrochemical exfoliation of layered black phosphorus into phosphorene. *Angew. Chem. Int. Ed.* **56**, 10443–10445 (2017).

67. Ambrosi, A., Sofer, Z., Luxa, J. & Pumera, M. Exfoliation of layered topological insulators Bi_2Se_3 and Bi_2Te_3 via electrochemistry. *ACS Nano* **10**, 11442–11448 (2016).
68. Ding, Y. et al. Controlled intercalation and chemical exfoliation of layered metal–organic frameworks using a chemically labile intercalating agent. *J. Am. Chem. Soc.* **139**, 9136–9139 (2017).
69. Peng, Y. et al. Metal–organic framework nanosheets as building blocks for molecular sieving membranes. *Science* **346**, 1356–1359 (2014).
70. Eda, G. et al. Coherent atomic and electronic heterostructures of single-layer MoS_2 . *ACS Nano* **6**, 7311–7317 (2012).
71. Hernandez, Y. et al. High-yield production of graphene by liquid-phase exfoliation of graphite. *Nat. Nanotechnol.* **3**, 563–568 (2008).
72. Chen, Y. et al. Phase engineering of nanomaterials. *Nat. Rev. Chem.* **4**, 243–256 (2020).
73. Li, W., Qian, X. & Li, J. Phase transitions in 2D materials. *Nat. Rev. Mater.* **6**, 829–846 (2021).
74. Xia, F., Wang, H., Xiao, D., Dubey, M. & Ramasubramanian, A. Two-dimensional material nanophotonics. *Nat. Photonics* **8**, 899–907 (2014).
75. Manzeli, S., Ovchinnikov, D., Pasquier, D., Yazyev, O. V. & Kis, A. 2D transition metal dichalcogenides. *Nat. Rev. Mater.* **2**, 17033 (2017).
76. Yang, H., Kim, S. W., Chhowalla, M. & Lee, Y. H. Structural and quantum-state phase transitions in van der Waals layered materials. *Nat. Phys.* **13**, 931–937 (2017).
77. Voiry, D., Mohite, A. & Chhowalla, M. Phase engineering of transition metal dichalcogenides. *Chem. Soc. Rev.* **44**, 2702–2712 (2015).
78. Kappera, R. et al. Phase-engineered low-resistance contacts for ultrathin MoS_2 transistors. *Nat. Mater.* **13**, 1128–1134 (2014).
79. Zhao, W., Ribeiro, R. M. & Eda, G. Electronic structure and optical signatures of semiconducting transition metal dichalcogenide nanosheets. *Acc. Chem. Res.* **48**, 91–99 (2015).
80. Zhou, Z. et al. Metallic 1T phase enabling MoS_2 nanodots as an efficient agent for photoacoustic imaging guided photothermal therapy in the near-infrared-II window. *Small* **16**, 2004173 (2020).
81. Fan, X. et al. Fast and efficient preparation of exfoliated 2H MoS_2 nanosheets by sonication-assisted lithium intercalation and infrared laser-induced 1T to 2H phase reversion. *Nano Lett.* **15**, 5956–5960 (2015).
82. Wang, Y. et al. Structural phase transition in monolayer MoTe_2 driven by electrostatic doping. *Nature* **550**, 487–491 (2017).
83. Li, Y., Duerloo, K.-A. N., Wauson, K. & Reed, E. J. Structural semiconductor-to-semimetal phase transition in two-dimensional materials induced by electrostatic gating. *Nat. Commun.* **7**, 10671 (2016).
84. Yu, Y. et al. Gate-tunable phase transitions in thin flakes of 1T- TaS_2 . *Nat. Nanotechnol.* **10**, 270–276 (2015).
85. Kumbhakar, P. et al. Emerging 2D metal oxides and their applications. *Mater. Today* **45**, 142–168 (2021).
86. Li, X. et al. Highly conducting graphene sheets and Langmuir–Blodgett films. *Nat. Nanotechnol.* **3**, 538–542 (2008).
87. Zhu, J. et al. Layer-by-layer assembled 2D montmorillonite dielectrics for solution-processed electronics. *Adv. Mater.* **28**, 63–68 (2016).
88. Zhu, J. et al. Solution-processed dielectrics based on thickness-sorted two-dimensional hexagonal boron nitride nanosheets. *Nano Lett.* **15**, 7029–7036 (2015).
89. Mei, L. et al. Simultaneous electrochemical exfoliation and covalent functionalization of MoS_2 membrane for ion sieving. *Adv. Mater.* **34**, 2201416 (2022).
90. Yan, Z. et al. Highly stretchable van der Waals thin films for adaptable and breathable electronic membranes. *Science* **375**, 852–859 (2022).
91. Zhu, C. et al. Single-layer MoS_2 -based nanoprobe for homogeneous detection of biomolecules. *J. Am. Chem. Soc.* **135**, 5998–6001 (2013).
92. Li, J., Zhan, G., Yu, Y. & Zhang, L. Superior visible light hydrogen evolution of Janus bilayer junctions via atomic-level charge flow steering. *Nat. Commun.* **7**, 11480 (2016).
93. Huang, J. et al. Electrochemical exfoliation of pillared-layer metal–organic framework to boost the oxygen evolution reaction. *Angew. Chem. Int. Ed.* **57**, 4632–4636 (2018).
94. Zhang, S. et al. MoS_2 quantum dot growth induced by S vacancies in a ZnIn_2S_4 monolayer: atomic-level heterostructure for photocatalytic hydrogen production. *ACS Nano* **12**, 751–758 (2018).
95. Shi, Y. et al. Van Der Waals gap-rich BiOCl atomic layers realizing efficient, pure-water CO_2 -to- CO photocatalysis. *Nat. Commun.* **12**, 5923 (2021).
96. Kang, J., Tongay, S., Zhou, J., Li, J. & Wu, J. Band offsets and heterostructures of two-dimensional semiconductors. *Appl. Phys. Lett.* **102**, 012111 (2013).
97. Li, X. et al. Ordered clustering of single atomic Te vacancies in atomically thin PtTe_2 promotes hydrogen evolution catalysis. *Nat. Commun.* **12**, 2351 (2021).
98. Lai, Z. et al. High-yield exfoliation of ultrathin 2D $\text{Ni}_3\text{Cr}_2\text{P}_2\text{S}_9$ and $\text{Ni}_3\text{Cr}_2\text{P}_2\text{Se}_9$ nanosheets. *Small* **17**, 2006866 (2021).
99. Mounet, N. et al. Two-dimensional materials from high-throughput computational exfoliation of experimentally known compounds. *Nat. Nanotechnol.* **13**, 246–252 (2018).
100. Morgan, D. et al. Machine learning in nuclear materials research. *Curr. Opin. Solid State Mater. Sci.* **26**, 100975 (2022).
101. Lin, Y.-C., Dumcenco, D. O., Huang, Y.-S. & Suenaga, K. Atomic mechanism of the semiconducting-to-metallic phase transition in single-layered MoS_2 . *Nat. Nanotechnol.* **9**, 391–396 (2014).
102. Xiong, F. et al. Li Intercalation in MoS_2 : in situ observation of its dynamics and tuning optical and electrical properties. *Nano Lett.* **15**, 6777–6784 (2015).
103. Yang, R. et al. Fabrication of liquid cell for in-situ transmission electron microscopy of electrochemical processes. *Nat. Protoc.* <https://doi.org/10.1038/s41596-022-00762-y> (2022).
104. Wang, C. et al. Monolayer atomic crystal molecular superlattices. *Nature* **555**, 231–236 (2018).
105. Zhai, X. et al. Direct observation of the light-induced exfoliation of molybdenum disulfide sheets in water medium. *ACS Nano* **15**, 5661–5670 (2021).
106. Kong, W. et al. Path towards graphene commercialization from lab to market. *Nat. Nanotechnol.* **14**, 927–938 (2019).
107. Walker, G. F. & Garrett, W. G. Chemical exfoliation of vermiculite and the production of colloidal dispersions. *Science* **156**, 385–387 (1967).
108. Murphy, D. W. & Hull, G. W. Jr Monodispersed tantalum disulfide and adsorption complexes with cations. *J. Chem. Phys.* **62**, 973–978 (1975).
109. Liu, C., Singh, O., Joensen, P., Curzon, A. E. & Frindt, R. F. X-ray and electron microscopy studies of single-layer TaS_2 and NbS_2 . *Thin Solid Films* **113**, 165–172 (1984).
110. Binnig, G., Rohrer, H., Gerber, C. & Weibel, E. Surface studies by scanning tunneling microscopy. *Phys. Rev. Lett.* **49**, 57–61 (1982).
111. Binnig, G., Quate, C. F. & Gerber, C. Atomic force microscope. *Phys. Rev. Lett.* **56**, 930–933 (1986).
112. Zhu, J. et al. Argon plasma induced phase transition in monolayer MoS_2 . *J. Am. Chem. Soc.* **139**, 10216–10219 (2017).

Acknowledgements

Z.Z. thanks the ECS scheme (CityU9048163) from RGC in Hong Kong and the Basic Research Project from the Shenzhen Science and Technology Innovation Committee in Shenzhen, China (No.

JCYJ20210324134012034). Q.L. thanks the Natural Sciences and Engineering Research Council of Canada (NSERC) Discovery Grant and the Alberta Innovates Advance Program-NSERC Alliance Grant.

Author contributions

Z.Z. proposed the topic of the Review. R.Y., J.L. and Z.Z. drafted the manuscript. H.S.S., D.V. and Q.L. revised the manuscript. Y.F. and L.M. contributed to the data collection for the manuscript.

Competing interests

The authors declare no competing interests.

Additional information

Supplementary information The online version contains supplementary material available at <https://doi.org/10.1038/s44160-022-00232-z>.

Correspondence should be addressed to Ju Li or Zhiyuan Zeng.

Peer review information *Nature Synthesis* thanks the anonymous reviewers for their contribution to the peer review of this work. Primary Handling Editor: Alexandra Groves, in collaboration with the *Nature Synthesis* team.

Reprints and permissions information is available at www.nature.com/reprints.

Publisher's note Springer Nature remains neutral with regard to jurisdictional claims in published maps and institutional affiliations.

Springer Nature or its licensor (e.g. a society or other partner) holds exclusive rights to this article under a publishing agreement with the author(s) or other rightsholder(s); author self-archiving of the accepted manuscript version of this article is solely governed by the terms of such publishing agreement and applicable law.

© Springer Nature Limited 2023

Synthesis of atomically thin sheets by the intercalation-based exfoliation of layered materials

In the format provided by the authors and unedited

Supplementary information

for

Synthesis of atomically thin sheets by the intercalation-based exfoliation of layered materials

Ruijie Yang^{1,2}, Yingying Fan^{1,2}, Liang Mei¹, Hyeon Suk Shin³, Damien Voiry⁴, Qingye Lu², Ju Li^{5†}, Zhiyuan Zeng^{1,6†}

¹Department of Materials Science and Engineering and State Key Laboratory of Marine Pollution, City University of Hong Kong, 83 Tat Chee Avenue, Kowloon, Hong Kong 999077, P. R. China.

²Department of Chemical and Petroleum Engineering, University of Calgary, 2500 University Drive, NW, Calgary, Alberta, T2N 1N4, Canada.

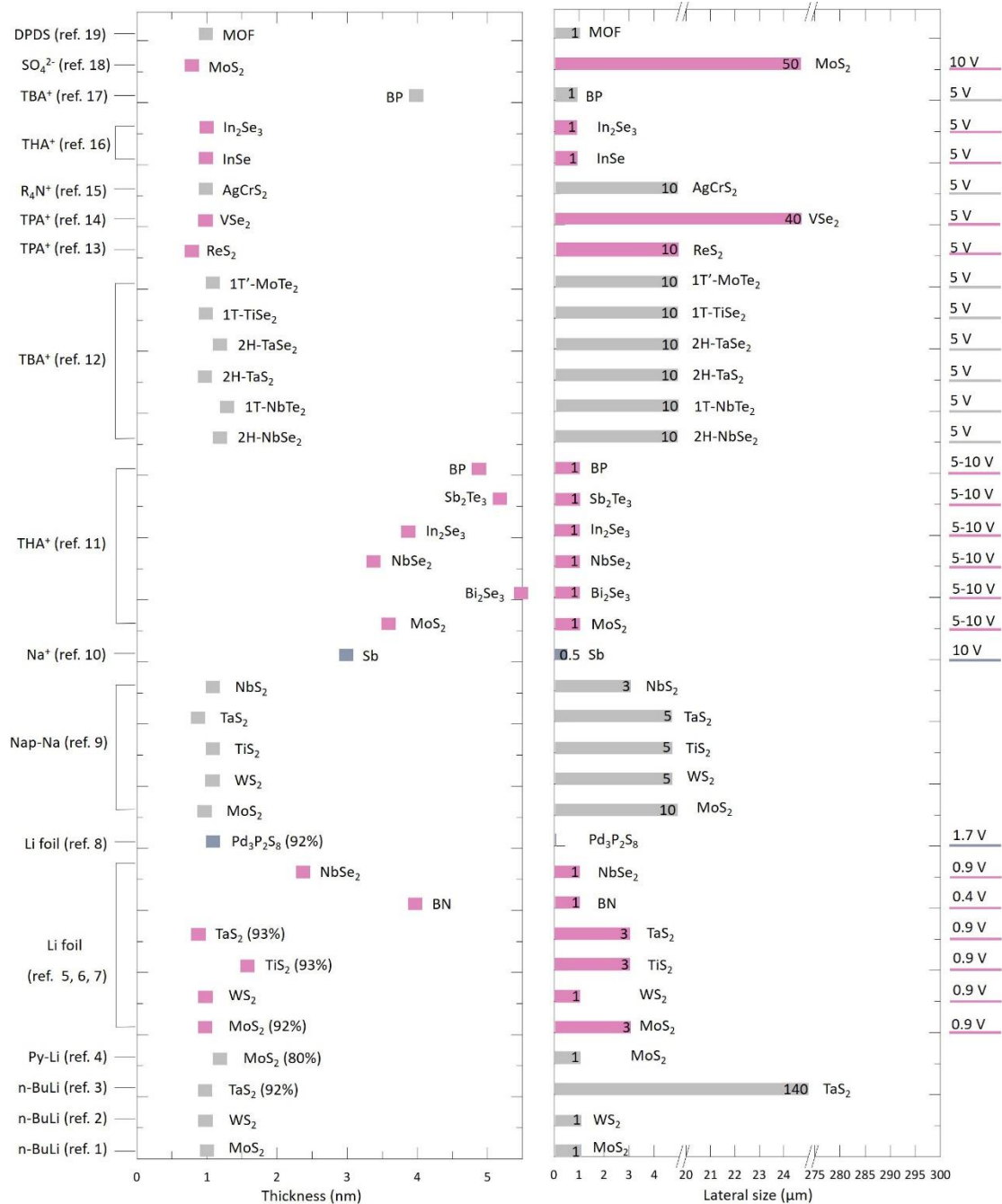
³Department of Chemistry, Ulsan National Institute of Science and Technology (UNIST), Ulsan 612022, South Korea.

⁴Institut Européen des Membranes, IEM, UMR 5635, Université Montpellier, ENSCM, CNRS, Montpellier.

⁵Department of Nuclear Science and Engineering and Department of Materials Science and Engineering, Massachusetts Institute of Technology, Cambridge, MA, 02139, USA.

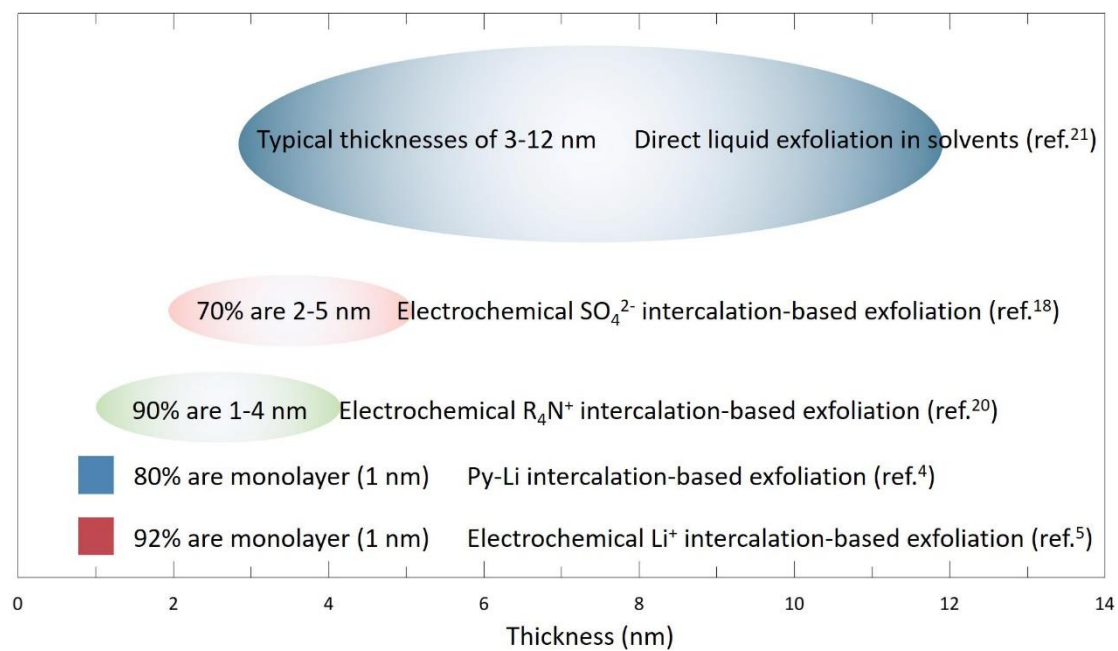
⁶Shenzhen Research Institute, City University of Hong Kong, Shenzhen 518057, China.

†E-mail: zhiyzeng@cityu.edu.hk, liju@mit.edu

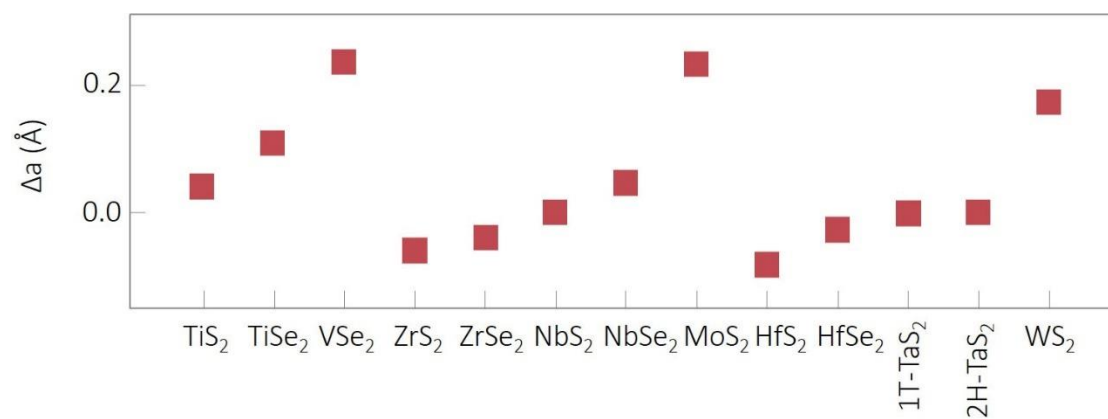


Supplementary Figure 1 | **Summary of product quality (thickness, yield, and lateral size) of various types of intercalation-based exfoliation methods.** Data collected from ref.¹⁻¹⁹. If the nanosheets are prepared by an electrochemical intercalation-based exfoliation method, the corresponding applied voltage values are listed on the right side of the figure. Of note, the quality of the final products (thickness, yield, lateral size, and others) prepared by intercalation-based exfoliation method is not only related to the intercalant used, but also may be affected by some other experimental conditions, including the applied voltage or current, exfoliation power (*e.g.*, ultrasonic power), etc.

(as shown in **Fig. 5e, f**). Crucially, the quality of the final product (of particular thickness and lateral size) can also be on-demand selected via adjusting the centrifugal speed (As shown in **Fig. 5g**). DPDS: 4,4'-Dipyridyl disulfide; SO_4^{2-} : Sulfate ion; TBA^+ : Tetrabutylammonium ion; THA^+ : Tetraheptylammonium ion; R_4N^+ : Tetraalkylammonium ion; TPA^+ : Tetrapropylammonium ion; Na^+ : Sodium ion; Nap-Na: Naphthalenide Sodium; Li foil: Lithium foil; Py-Li: pyrene lithium; *n*-BuLi: *n*-Butyllithium.

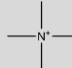
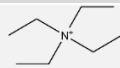
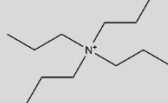
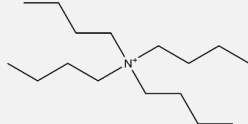
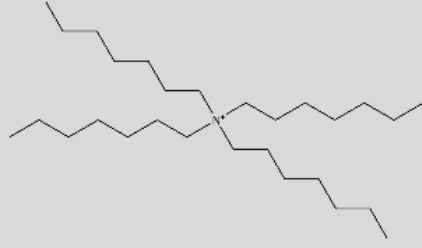
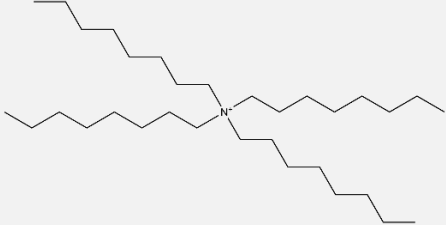


Supplementary Figure 2 | **Comparison of product (take MoS₂ as an example) thickness of intercalation-based exfoliation method and direct liquid exfoliation method.** Data collected from ref.^{4,5,18,20,21}.



Supplementary Figure 3 | **D-value (difference value) of lattice parameter a (Δa) of 13 kinds of TMD materials.** Adapted with permission from ref.³, American Chemical Society.

Supplementary Table 1 | **A list of tetraalkylammonium cations (R_4N^+) used for the electrochemical intercalation-based exfoliation strategy.**

| Abbreviation | Full name | Structural formula |
|------------------|-------------------------|--|
| TMA ⁺ | Tetramethylammonium ion |  |
| TEA ⁺ | Tetraethylammonium ion |  |
| TPA ⁺ | Tetrapropylammonium ion |  |
| TBA ⁺ | Tetrabutylammonium ion |  |
| THA ⁺ | Tetraheptylammonium ion |  |
| TOA ⁺ | Tetraoctylammonium ion |  |

Supplementary Table 2 | **Examples of device applications of exfoliated nanosheets.**

| Nanosheet | Intercalation-based exfoliation (IE) method | Deposition technique | Substrate | Device | Performance | Ref. |
|------------------|--|------------------------------------|---|-----------------------|--|------|
| Graphene | Electrochemical SO ₄ ²⁻ IE | Dip-coating | Si/SiO ₂ | FET | Field-effect mobility of 17 cm ² ·V ⁻¹ ·s ⁻¹ | 22 |
| | Electrochemical SO ₄ ²⁻ IE | Vacuum filtration and dry transfer | PTFE membrane transfer to Si/SiO ₂ | FET | High hole mobility of ~233 cm ² ·V ⁻¹ ·s ⁻¹ | 23 |
| | Electrochemical SO ₄ ²⁻ IE | Brush painting | Commercial A4-size paper | Supercapacitor | High area capacitance of 11.3 mF·cm ⁻² , excellent rate capability of 5000 mV·s ⁻¹ . | 24 |
| | Electrochemical BF ₄ ⁻ IE | Vacuum filtration and dry transfer | PTFE membrane transfer to PET | Supercapacitor | High energy density of 56 mWh·cm ⁻³ | 25 |
| MoS ₂ | Electrochemical SO ₄ ²⁻ IE | Dip-coating | Si/SiO ₂ | FET | On/off current ratio of 10 ⁶ , field-effect mobility of 1.2 cm ² ·V ⁻¹ ·s ⁻¹ | 18 |
| | Chemical Li ⁺ IE | Vacuum filtration | Nylon supports with 200 nm pore size | Nanolaminate membrane | >90% and ~87% rejection rates for micropollutants and NaCl, respectively | 26 |
| | Chemical Li ⁺ IE | Vacuum filtration | Porous PES with 30 nm pore size | Nanolaminate membrane | >90% rejection rates for micropollutants | 27 |

| | | | | | |
|-------------------------------------|--------------------------------|---|-----------------------|--|----|
| Chemical Li ⁺ IE | Vacuum filtration | Cellulose ester with 25 nm pore size | Nanolaminate membrane | ~92% rejection rates for Na ₂ SO ₄ | 28 |
| Electrochemical Li ⁺ IE | Vacuum filtration | Nylon supports with 220 nm pore size | Nanolaminate membrane | >90% and >80% rejection rates for various dyes and NaCl, respectively | 29 |
| Electrochemical Li ⁺ IE | Vacuum filtration and transfer | Cellulose acetate filter membrane transfer to polyimide | Supercapacitor | High areal capacitance of 0.63 F·cm ⁻² , volumetric capacitance of 437 F·cm ⁻³ | 30 |
| Chemical Li ⁺ IE | Vacuum filtration and transfer | Nitrocellulose membranes transfer to polyimide | Supercapacitor | Capacitance values ranging from ~400 to ~700 F·cm ⁻³ in a variety of aqueous electrolytes | 31 |
| Chemical Li ⁺ IE | - | - | Lithium ion battery | Initial charge and discharge capacities are as much as 1113.3/2084.4 mAh·g ⁻¹ | 4 |
| Chemical Li ⁺ IE | - | Si/SiO ₂ | Photodetector | The responsivity and detectivity of the MoS ₂ based photodetector are 0.881 mA/W and 1.28 × 10 ⁹ Jones at 980 nm and 0.539 mA/W and 0.94 × 10 ⁹ Jones at 1550 nm, respectively. | 32 |
| Electrochemical THA ⁺ IE | Spin-coating | Si/SiO ₂ | TFT | Room-temperature mobilities of about 10 square centimetres per volt per second and on/off ratios of 10 ⁶ | 11 |

| | | | | | | |
|---------------------------------|-------------------------------------|------------------------------------|---|-------------------------|---|----|
| TaS ₂ | Chemical Li ⁺ IE | Vacuum filtration and transfer | Cellulose acetate membrane transfer to glass | Supercapacitor | Large volumetric capacitance of 508 F·cm ⁻³ at scan rate of 10 mV·s ⁻¹ and high energy density of 58.5 Wh·L ⁻¹ | 33 |
| WS ₂ | Chemical Li ⁺ IE | Vacuum filtration | AAO membrane with a pore size of 200 nm | Nanolaminate membrane | 93% rejection for EB and 98% for cyt <i>c.</i> | 34 |
| | Chemical Li ⁺ IE | Vacuum filtration | Filter membrane | Photodetector | Broadband wavelength from visible light to near-infrared light (532–1064 nm), the responsivity is 4.04 mA/W, and the detectivity is 2.55 × 10 ⁹ Jones at 532 nm irradiation. | 35 |
| MoTe ₂ | Electrochemical THA ⁺ IE | Spin-coating | Si/SiO ₂ | Fiber ring laser cavity | Repetition rate of 3.15 MHz and pulse duration as short as 867 fs at 1563 nm | 36 |
| BP | Electrochemical TBA ⁺ IE | Dip-coating | Si/SiO ₂ | FET | High hole mobility of 76 cm ² ·V ⁻¹ ·s ⁻¹ and an on/off ratio of 10 ³ at 298 K | 37 |
| | Electrochemical TBA ⁺ IE | Spin-coating | Si/SiO ₂ | FET | High hole mobility of 252 ± 18 cm ² ·V ⁻¹ ·s ⁻¹ and a remarkable on/off ratio of (1.2 ± 0.15) × 10 ⁵ at 143 K | 17 |
| | Electrochemical TBA ⁺ IE | Drop-coating | Si/SiO ₂ | FET | High mean hole mobility of ~60 cm ² ·V ⁻¹ ·s ⁻¹ (up to ~100 cm ² ·V ⁻¹ ·s ⁻¹) with a high on/off ratio (~1 × 10 ⁴ in average) | 38 |
| In ₂ Se ₃ | Electrochemical THA ⁺ IE | Vacuum filtration and dry transfer | PTFE membrane transfer to Si/SiO ₂ | Photodetector | Ultrafast response time with a rise and decay of 41 and 39 ms, respectively, and efficient responsivity of 1 mA·W ⁻¹ | 39 |

| | | | | | | |
|---------------------------------|--|--------------|---------------------|---------------|--|----|
| | Electrochemical THA ⁺ IE | Spin-coating | Si/SiO ₂ | FET | An on/off ratio of more than 10 ⁵ and electron mobility of 0.2 cm ² ·V ⁻¹ ·s ⁻¹ | 16 |
| InSe | Electrochemical TBA ⁺ IE | Drop-casting | FTO | Photodetector | The photoresponse and response time are 10.14 mA/W and 2/37 ms, respectively. | 40 |
| Bi ₂ Se ₃ | Chemical Li ⁺ IE | - | ITO | Photodetector | The response time and responsivity are about 0.7 s, and 20.48 mA/W, respectively. | 41 |

IE: Intercalation-based exfoliation

FET: Field effect transistor

PTFE: Polytetrafluoroethylene

PET: Polyethylene terephthalate

PES: Poly(ether sulfone)

TFT: Thin-film transistor

AAO: Anodic alumina oxide

EB: Evans Blue

cyt *c*: cytochrome *c*

FTO: SnO₂:F

ITO: Indium–tin oxide

Supplementary Table 3 | **Examples of catalysis applications of exfoliated nanosheets.**

| Nanosheet | Intercalation-based exfoliation (IE) method | Application | Performance | Ref. |
|---|---|-------------------------------------|---|------|
| MoS ₂ | Chemical Li ⁺ IE | Electrocatalytic HER | Electrocatalytic current density of 10 mA·cm ⁻² at a low overpotential of -187 mV vs RHE and a Tafel slope of 43 mV/decade | 42 |
| WS ₂ | Chemical Li ⁺ IE | Electrocatalytic HER | The TOF reaches 175 s ⁻¹ at a potential of -288 mV | 2 |
| Pd ₃ P ₂ S ₈ | Electrochemical Li ⁺ IE | Electrocatalytic HER | Onset potential of -52 mV, a Tafel slope of 29 mV dec ⁻¹ | 8 |
| Sb | Electrochemical Na ⁺ IE | Electrocatalytic CO ₂ RR | FE for formate of 88.5 % at a potential of -0.96 V | 10 |
| ZnIn ₂ S ₄ | Chemical Li ⁺ IE | Photocatalytic HER | 2.258 mmol·g ⁻¹ ·h ⁻¹ | 43 |
| BiOCl | Electrochemical Li ⁺ IE | Photocatalytic CO ₂ RR | 0.1882 mmol·g ⁻¹ ·h ⁻¹ | 44 |

IE: Intercalation-based exfoliation









HER: Hydrogen evolution reaction





CO₂RR: CO₂ reduction reaction











TOF: Turnover frequency








FE: Faraday efficiency

Supplementary Table 4 | **Price list of layered materials. Data and pictures collected from hq-graphene (<http://www.hqgraphene.com/index.php>).**

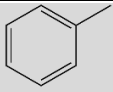
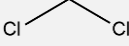
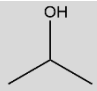
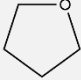
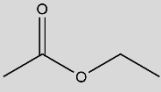
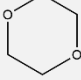
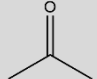
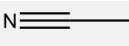
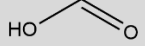
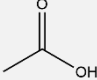
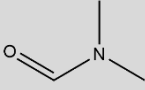
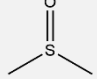
| Layered materials | Lateral size | Photograph | Price (euro) |
|---|--------------|---|--------------|
| MoS ₂ (2H Molybdenum Disulfide) | 0.8-1 cm |  | 635 |
| MoSe ₂ (2H Molybdenum Diselenide) | 0.8-1 cm |  | 635 |
| MoTe ₂ (2H Molybdenum Ditelluride) | 0.6-0.8 cm |  | 635 |
| WS ₂ (2H Tungsten Disulfide) | 0.8-1 cm |  | 635 |
| WSe ₂ (Tungsten Diselenide) | 0.8-1 cm |  | 635 |
| WTe ₂ (Tungsten Ditelluride) | 0.6-0.8 cm |  | 635 |
| TiS ₂ (1T Titanium Disulfide) | 0.6-0.8 cm |  | 635 |
| TiSe ₂ (1T Titanium Diselenide) | 0.8 cm |  | 635 |

| | | | |
|--|------------|---|-----|
| TiTe ₂ (Titanium Ditelluride) | 0.8 cm |  | 635 |
| ZrSe ₃ (Zirconium Triselenide) | 0.6-0.8 cm |  | 635 |
| ZrSe ₂ (Zirconium Diselenide) | 0.8-1 cm |  | 635 |
| ZrTe ₃ (Zirconium Tritelluride) | 0.6-0.8 cm |  | 635 |
| TaS ₂ (2H Tantalum Disulfide) | 0.6-0.8 cm |  | 635 |
| TaSe ₂ (2H Tantalum Diselenide) | 0.6-0.8 cm |  | 635 |
| TaTe ₂ (Tantalum Ditelluride) | 0.6-0.8 cm |  | 635 |
| NbS ₂ (3R Niobium Disulfide) | 0.4 cm |  | 635 |
| NbSe ₂ (2H Niobium Diselenide) | 0.6-0.8 cm |  | 635 |
| NbTe ₂ (Niobium Ditelluride) | 0.6-0.8 cm |  | 635 |

| | | | |
|--|------------|---|-----|
| HfS ₂ (Hafnium Disulfide) | 0.6-0.8 cm |  | 635 |
| HfSe ₂ (Hafnium Diselenide) | 0.6-0.8 cm |  | 635 |
| HfTe ₂ (1T Hafnium Ditelluride) | 0.6-0.8 cm |  | 635 |
| VSe ₂ (1T Vanadium Diselenide) | 0.6-0.8 cm |  | 635 |
| ReS ₂ (Rhenium Disulfide) | 0.8 cm |  | 635 |
| ReSe ₂ (Rhenium Diselenide) | 0.6-0.8 cm |  | 635 |
| PtSe ₂ (Platina Diselenide) | 0.2-0.3 cm |  | 635 |
| PtTe ₂ (Platina Ditelluride) | 0.2-0.3 cm |  | 635 |
| SnS ₂ (2H Tin Disulfide) | 0.6-0.8 cm |  | 635 |
| SnSe ₂ (Tin Diselenide) | 0.8 cm |  | 635 |

| | | | |
|---|------------|---|-----|
| PdTe ₂ (Palladium Ditelluride) | 0.2-0.3 cm |  | 635 |
| Bi ₂ S ₃ (Bismuth Sulfide) | 0.6-0.8 cm |  | 635 |
| Bi ₂ Se ₃ (Bismuth Selenide) | 0.6-0.8 cm |  | 635 |
| Bi ₂ Te ₃ (Bismuth Telluride) | 0.6-0.8 cm |  | 635 |
| Natural graphite | 0.1 cm |  | 180 |
| h-BN (Hexagonal Boron Nitride) | 100 μm |  | 635 |
| BP (Black Phosphorus) | 0.6-0.8 cm |  | 690 |

Supplementary Table 5 | A list of solvents used for the dispersion of NbSe₂¹².

| Abbreviation | Full name | Structural formula | Polarity Index |
|--------------|------------------------|--|----------------|
| TOL | Toluene |  | 2.4 |
| DCM | Dichloromethane |  | 3.1 |
| IPA | Isopropyl Alcohol |  | 4.0 |
| THF | Tetrahydrofuran |  | 4.0 |
| ETAC | Ethyl Acetate |  | 4.4 |
| DIOX | 1,4-Dioxane |  | 4.8 |
| ACE | Acetone |  | 5.1 |
| ACN | Acetonitrile |  | 5.8 |
| FA | Formic Acid |  | 6.0 |
| AA | Acetic Acid |  | 6.0 |
| DMF | N,N-Dimethyl Formamide |  | 6.4 |
| DMSO | Dimethyl Sulfoxide |  | 7.2 |

References

- 1 Eda, G. *et al.* Photoluminescence from Chemically Exfoliated MoS₂. *Nano Lett.* **11**, 5111-5116 (2011).
- 2 Voiry, D. *et al.* Enhanced catalytic activity in strained chemically exfoliated WS₂ nanosheets for hydrogen evolution. *Nat. Mater.* **12**, 850-855 (2013).
- 3 Peng, J. *et al.* Very Large-Sized Transition Metal Dichalcogenides Monolayers from Fast Exfoliation by Manual Shaking. *J. Am. Chem. Soc.* **139**, 9019-9025 (2017).
- 4 Zhu, X. *et al.* Exfoliation of MoS₂ Nanosheets Enabled by a Redox-Potential-Matched Chemical Lithiation Reaction. *Nano Lett.* **22**, 2956-2963 (2022).
- 5 Zeng, Z. *et al.* Single-Layer Semiconducting Nanosheets: High-Yield Preparation and Device Fabrication. *Angew. Chem. Int. Edit.* **50**, 11093-11097 (2011).
- 6 Zeng, Z. *et al.* An Effective Method for the Fabrication of Few-Layer-Thick Inorganic Nanosheets. *Angew. Chem. Int. Edit.* **51**, 9052-9056 (2012).
- 7 Yang, R. *et al.* High-yield production of mono- or few-layer transition metal dichalcogenide nanosheets by an electrochemical lithium ion intercalation-based exfoliation method. *Nat. Protoc.* **17**, 358-377 (2022).
- 8 Zhang, X. *et al.* Lithiation-induced amorphization of Pd₃P₂S₈ for highly efficient hydrogen evolution. *Nat. Catal.* **1**, 460-468 (2018).
- 9 Zheng, J. *et al.* High yield exfoliation of two-dimensional chalcogenides using sodium naphthalenide. *Nat. Commun.* **5**, 2995 (2014).
- 10 Li, F. *et al.* Unlocking the Electrocatalytic Activity of Antimony for CO₂ Reduction by Two-Dimensional Engineering of the Bulk Material. *Angew. Chem. Int. Edit.* **56**, 14718-14722 (2017).
- 11 Lin, Z. *et al.* Solution-processable 2D semiconductors for high-performance large-area electronics. *Nature* **562**, 254-258 (2018).
- 12 Li, J. *et al.* Printable two-dimensional superconducting monolayers. *Nat. Mater.* **20**, 181-187 (2021).

- 13 Yu, W. *et al.* Domain Engineering in ReS₂ by Coupling Strain during Electrochemical Exfoliation. *Adv. Funct. Mater.* **30**, 2003057 (2020).
- 14 Yu, W. *et al.* Chemically Exfoliated VSe₂ Monolayers with Room-Temperature Ferromagnetism. *Adv. Mater.* **31**, 1903779 (2019).
- 15 Peng, J. *et al.* Stoichiometric two-dimensional non-van der Waals AgCrS₂ with superionic behaviour at room temperature. *Nat. Chem.* **13**, 1235-1240 (2021).
- 16 Lin, Z. *et al.* High-yield exfoliation of 2D semiconductor monolayers and reassembly of organic/inorganic artificial superlattices. *Chem* **7**, 1887-1902 (2021).
- 17 Yang, S. *et al.* A Delamination Strategy for Thinly Layered Defect-Free High-Mobility Black Phosphorus Flakes. *Angew. Chem. Int. Edit.* **57**, 4677-4681 (2018).
- 18 Liu, N. *et al.* Large-Area Atomically Thin MoS₂ Nanosheets Prepared Using Electrochemical Exfoliation. *ACS Nano* **8**, 6902-6910 (2014).
- 19 Ding, Y. *et al.* Controlled Intercalation and Chemical Exfoliation of Layered Metal–Organic Frameworks Using a Chemically Labile Intercalating Agent. *J. Am. Chem. Soc.* **139**, 9136-9139 (2017).
- 20 Tang, B. *et al.* Wafer-scale solution-processed 2D material analog resistive memory array for memory-based computing. *Nat. Commun.* **13**, 3037 (2022).
- 21 Coleman, J. N. *et al.* Two-Dimensional Nanosheets Produced by Liquid Exfoliation of Layered Materials. *Science* **331**, 568-571 (2011).
- 22 Su, C.-Y. *et al.* High-Quality Thin Graphene Films from Fast Electrochemical Exfoliation. *ACS Nano* **5**, 2332-2339 (2011).
- 23 Parvez, K. *et al.* Electrochemically Exfoliated Graphene as Solution-Processable, Highly Conductive Electrodes for Organic Electronics. *ACS Nano* **7** (2013).
- 24 Parvez, K. *et al.* Exfoliation of Graphite into Graphene in Aqueous Solutions of Inorganic Salts. *J. Am. Chem. Soc.* **136**, 6083-6091 (2014).
- 25 Zhou, F. *et al.* Electrochemically Scalable Production of Fluorine-Modified Graphene for Flexible and High-Energy Ionogel-Based Microsupercapacitors.

- J. Am. Chem. Soc.* **140**, 8198-8205 (2018).
- 26 Ries, L. *et al.* Enhanced sieving from exfoliated MoS₂ membranes via covalent functionalization. *Nat. Mater.* **18**, 1112-1117 (2019).
- 27 Wang, Z. *et al.* Understanding the Aqueous Stability and Filtration Capability of MoS₂ Membranes. *Nano Lett.* **17**, 7289-7298 (2017).
- 28 Hoenig, E. *et al.* Controlling the Structure of MoS₂ Membranes via Covalent Functionalization with Molecular Spacers. *Nano Lett.* **20**, 7844-7851 (2020).
- 29 Mei, L. *et al.* Simultaneous Electrochemical Exfoliation and Covalent Functionalization of MoS₂ Membrane for Ion Sieving. *Adva. Mater.* **34**, 2201416 (2022).
- 30 Chen, W. *et al.* Two-dimensional quantum-sheet films with sub-1.2 nm channels for ultrahigh-rate electrochemical capacitance. *Nat. Nanotechnol.* **17**, 153-158 (2022).
- 31 Acerce, M., Voiry, D. & Chhowalla, M. Metallic 1T phase MoS₂ nanosheets as supercapacitor electrode materials. *Nat. Nanotechnol.* **10**, 313-318 (2015).
- 32 Park, M. J., Park, K. & Ko, H. Near-infrared photodetector achieved by chemically-exfoliated multilayered MoS₂ flakes. *Appl. Surf. Sci.* **448**, 64-70 (2018).
- 33 Wu, J. *et al.* Acid-Assisted Exfoliation toward Metallic Sub-nanopore TaS₂ Monolayer with High Volumetric Capacitance. *J. Am. Chem. Soc.* **140**, 493-498 (2018).
- 34 Sun, L. *et al.* Ultrafast Molecule Separation through Layered WS₂ Nanosheet Membranes. *ACS Nano* **8**, 6304-6311 (2014).
- 35 Li, J., Han, J., Li, H., Fan, X. & Huang, K. Large-area, flexible broadband photodetector based on WS₂ nanosheets films. *Mat. Sci. Semicon. Proc.* **107**, 104804 (2020).
- 36 Yu, W. *et al.* High-Yield Exfoliation of Monolayer 1T'-MoTe₂ as Saturable Absorber for Ultrafast Photonics. *ACS Nano* **15**, 18448-18457 (2021).
- 37 Wang, N. *et al.* Electrochemical Delamination of Ultralarge Few-Layer Black Phosphorus with a Hydrogen-Free Intercalation Mechanism. *Adv. Mater.* **33**,

- 2005815 (2021).
- 38 Li, J. *et al.* Ultrafast Electrochemical Expansion of Black Phosphorus toward High-Yield Synthesis of Few-Layer Phosphorene. *Chem. Mater.* **30**, 2742-2749 (2018).
- 39 Shi, H. *et al.* Ultrafast Electrochemical Synthesis of Defect-Free In₂Se₃ Flakes for Large-Area Optoelectronics. *Adv. Mater.* **32**, 1907244 (2020).
- 40 Yang, X. *et al.* Boosting Photoresponse of Self-Powered InSe-Based Photoelectrochemical Photodetectors via Suppression of Interface Doping. *ACS Nano* **16**, 8440-8448 (2022).
- 41 Zang, C. *et al.* Photoresponse properties of ultrathin Bi₂Se₃ nanosheets synthesized by hydrothermal intercalation and exfoliation route. *Appl. Surf. Sci.* **316**, 341-347 (2014).
- 42 Lukowski, M. A. *et al.* Enhanced Hydrogen Evolution Catalysis from Chemically Exfoliated Metallic MoS₂ Nanosheets. *J. Am. Chem. Soc.* **135** (2013).
- 43 Zhang, S. *et al.* MoS₂ Quantum Dot Growth Induced by S Vacancies in a ZnIn₂S₄ Monolayer: Atomic-Level Heterostructure for Photocatalytic Hydrogen Production. *ACS Nano* **12**, 751-758 (2018).
- 44 Shi, Y. *et al.* Van Der Waals gap-rich BiOCl atomic layers realizing efficient, pure-water CO₂-to-CO photocatalysis. *Nat. Commun.* **12**, 5923 (2021).